applied sciences

MDPI

Article

A Generalized Nonlinear Beam Element for Slender RC Members Using a Polygonization Section Approach—Part I: Theoretical Formulation

Dimitris K. Sfondylis and Manolis G. Sfakianakis *

Department of Civil Engineering, University of Patras, 265 00 Patras, Greece; sfondylis.dimitris@gmail.com
* Correspondence: mgs@upatras.gr

Featured Application: Inelastic analysis of RC slender beam elements under cyclic loading.

Abstract: A mathematical model for RC beam elements is presented that falls into the category of distributed inelasticity models discretizing the cross-section in polygons (trapezoids, triangles). The models falling into these categories are considered to be able to describe in the best manner the inelastic behavior of the element across its whole clear length, since its response results from the numerical integration of the stiffnesses of its cross-sections, while presenting an ideal combination of accuracy, simplicity, and computational cost. The behavior of the cross-section is described through the constitutive relationships σ–ε of its materials for cyclic loading. The main objectives for the development of the proposed mathematical model are as follows: (a) the increased accuracy of the results compared to existing experimental ones; (b) the limitless generalization of its application, regarding of the cross-section shape; and (c) the elimination of the numerical problems presented by the application of other related models, a fact that leads to their impractical use in real three-dimensional structures. The proposed model falls under the category of distributed inelasticity models. This paper focuses on its initial version, which targets slender beam elements with negligible shear and bond-slip effects (i.e., with ribbed bars, sufficiently anchored). Thus, it is applicable to 2D and 3D framed structures that fulfill these conditions, while its modular structure allows for future adjustments for the inclusion of other effects.

Keywords: bending with axial load; FEM mathematical model; inelastic analysis of RC structures; reinforced concrete; RC fiber model; RC random cross-section shape

check for updates

Citation: Sfondylis, D.K.; Sfakianakis, M.G. A Generalized Nonlinear Beam Element for Slender RC Members Using a Polygonization Section Approach—Part I: Theoretical Formulation. *Appl. Sci.* **2024**, *14*, 2188. https://doi.org/10.3390/app14052188

Academic Editors: Rosario Montuori, Kang Su Kim and Francesco Clementi

Received: 17 August 2023
Revised: 11 February 2024
Accepted: 26 February 2024
Published: 5 March 2024

Copyright: © 2024 by the authors. Licensee MDPI, Basel, Switzerland. This article is an open access article distributed under the terms and conditions of the Creative Commons Attribution (CC BY) license (https://creativecommons.org/licenses/by/4.0/).

1. Introduction

The finite element method (FEM) is a well-established computational method used in the field of structural analysis. According to this method, a framed structure is represented as a set of connected beam-like elements used to describe the response of the corresponding real RC members (beams and columns). The constitutive laws of plasticity are assigned to these elements, either at the member level (as phenomenological rules expressed in terms of moment–curvature, M–φ, concentrated at its ends), or at the cross-sectional level (distributed along the element's axis and expressed in terms of stress–strain laws, σ–ε, of its materials). These approaches correspond to two categories of inelastic models: those of concentrated response and those of distributed inelastic response.

Distributed plasticity models are considered to be more accurate than the concentrated ones. According to the first models, elements can behave inelastically not only at their ends but also in between their end nodes. The inelastic behavior is initially calculated at the cross-sectional level, while the whole element's response results from the numerical integration of the responses of a predefined number of control cross-sections, defined appropriately along the member's clear length.

Coming to the cross-section's inelastic behavior, according to the well-known fiber model approach, a section is usually discretized into a large number of material fibers each adopting uniaxial behavior. The response of each material fiber is calculated in terms of its uniaxial constitutive stress–strain law, σ–ε, using Navier–Bernoulli's classic hypothesis of plane cross-sections after bending. The resultant internal forces of the cross-section are derived from the integration of the stresses of all its fibers.

An alternative approach to that of the fiber models, which is used in the proposed model, is to discretize the section into a number of polygons, mainly trapezoids and triangles, and to compute their inelastic responses in a similar manner to that of the fibers, as will be described in the following sections.

Historically, two categories of finite element formulations have been used: the stiffness method and the flexibility method. In the flexibility method (also known as the force method), flexibilities appear in the equations of compatibility and forces are the unknown quantities. On the other hand, in the stiffness method (also known as displacement method), displacements are the unknown quantities. Typical models using the stiffness method are those of Hellesland and Scordelis [1] and Mari and Scordelis [2], which use cubic polynomials as interpolation functions to approach the distribution of displacements along the length of the member.

The flexibility method was first followed by Mahasuverachai and Powell [3], using interpolation functions that are updated at each step, depending on the degree of inelasticity, for cross-sections under uniaxial bending. Zeris and Mahin [4] created a similar model for biaxial bending where the sections' stiffnesses also change and adapt according to the degree of inelasticity in the current step of the analysis. Moreover, they applied some improvements to the member-equilibrium calculation process in order to improve convergence.

Taucer et al. [5] and Spacone et al. [6–8] developed a mixed-formulation method combining stiffness and flexibility methods. The element-state determination process is based on the stiffness method, while the element-flexibility matrix is calculated by integrating the respective flexibility matrices of the control sections along the element length. They suggest a more transparent iterative process to perform the element-state determination at each step of the imposed displacements. According to this formulation, the element's equilibrium is always satisfied (based on computational limits), and the model can converge after a few iterations, satisfying the constitutive laws of the fibers of the materials. It does not require a large number of control sections along the length of the member. It also proves to be relatively stable compared to previous models mentioned above, especially for RC sections subjected to very high inelastic stress–strain conditions.

Monti and Spacone [9] extended the model of Taucer et al. [5] to take into account the bond-slip phenomenon. Kagermanov and Ceresa [10] proposed a model based on the stiffness-method formulation, which uses a triaxial constitutive law for concrete. Bairan and Mari [11] developed another formulation of the fiber model that takes into account shear and torsion phenomena. In this formulation, the displacement field is extended by adding a torsional field. At the same time, the fiber state is calculated in the three-dimensional space using a three-dimensional constitutive law for concrete. Finally, Kashani et al. [12] presented a fiber model that takes into account the buckling of reinforcing bars for the circular cross-sections of bridge pillars.

Coming to the proposed model [13], it belongs to the general category of the distributed inelasticity models for the inelastic response of slender RC-beam elements subjected to cyclic bending with axial force. The main target of the model is its applicability for the inelastic response of RC beams and columns, regardless of their cross-sectional shape, the position of longitudinal reinforcement bars, the possible presence of holes or exterior concrete-strengthening jacket, etc. Special computational care is given for the accurate description of the 3D shape of the concrete compressive-stress shell that, in general, acts in a random cross-section shape under a specific deformation profile. The detailed and accurate description of these stresses leads to the best approximation of the experimental

results. On the other hand, it proves to contribute significantly to the numerical stability of the model, as will be described in the following.

A model is considered stable if convergence is achieved in each loading step, meaning that the applied forces are balanced by the internal resisting forces. Many models suffer from numerical instabilities as described in Section 6.1.4, thus reducing their practical applicability.

For the present model, the limitations mentioned in the abstract are applied, while the influence of the speed of deformation (strain rate effect) during dynamic loading of shock type is not taken into consideration.

The concepts described in the following sections are as follows: the concrete and steel constitutive laws used in the model, the general FEM-formulation that is adopted, the cross-sectional-discretization process, and the overall numerical algorithm of the model along with its significant computational characteristics.

2. Concrete Constitutive Stress–Strain Law

The proposed model incorporates the concrete constitutive stress–strain law of Martinez-Rueda and Elnashai [14], which is an extension of the corresponding Mander's law [15]. Mander's model is considered the most widely acceptable model for concrete, while the modifications proposed by Martinez-Rueda and Elnashai enhance its numerical stability and robustness. Both of these models are widely used in commercial FEM software like ANSYS, SAP2000, etc.

This law consists of a uniaxial model for the behavior of confined or unconfined concrete under cyclic loading, while the tensile strength of concrete is neglected. The loading-unloading-reloading branches, as well as the branch-transition criteria of the initial Mander's model, have been appropriately modified.

The constitutive law of Martinez-Rueda and Elnashai [14] is based on two observations. First, the stress–strain envelope curve of concrete under cyclic load is almost identical to the stress–strain curve obtained from monotonic loading. Secondly, all loading, unloading and reloading branches (in blue color) have a common intersection point, called the "epicenter" point (ε_f, f_f), as shown in Figure 1. It is defined as the common point of the extended dashed lines which connect the unloading points with those of remaining plastic strains.

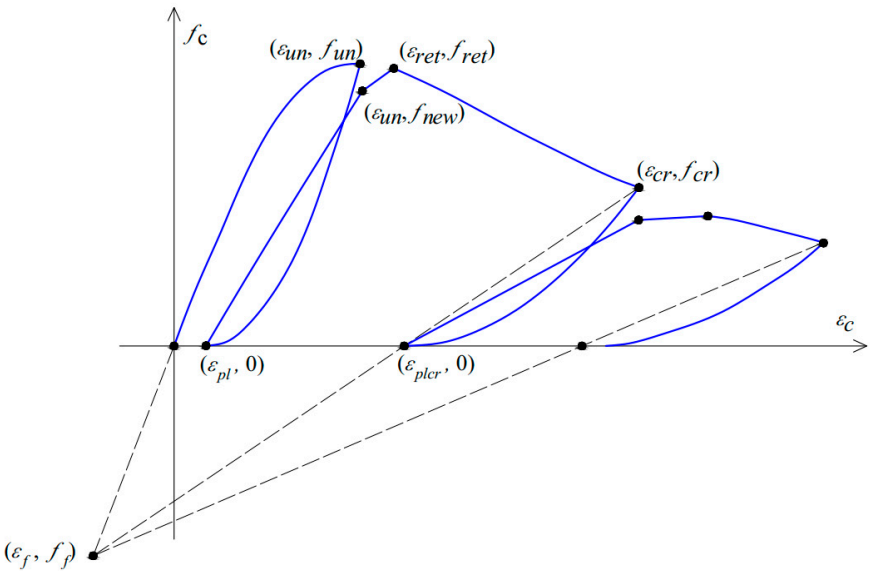

Figure 1. Loading-Unloading-Reloading branches of Martinez-Rueda and Elnashai [14] model.

The adopted concrete model consists of one loading, one unloading, and two reloading branches. The loading branch follows the monotonical stress–strain relationship of concrete (Figure 2), which is described by the following equations,

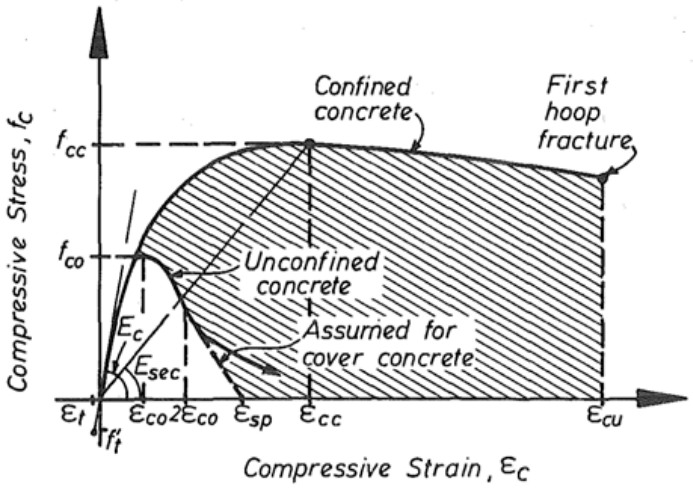

Figure 2. Stress–strain monotonic curve of confined and unconfined concrete—Mander et al. [15].

$$f_c = \frac{f_{cc} \cdot x \cdot r}{r - 1 + x^r} \tag{1}$$

$$f_{cc} = k \cdot f_{co} \tag{2}$$

$$x = \varepsilon_c / \varepsilon_{cc} \tag{3}$$

$$\varepsilon_{cc} = \varepsilon_{co}\left[1 + 5\left(\frac{f_{cc}}{f_{co}} - 1\right)\right] \tag{4}$$

$$r = \frac{E_c}{E_c - E_{\text{sec}}} \tag{5}$$

$$E_c(\text{MPa}) = 5000\sqrt{f_{co}(\text{MPa})} \tag{6}$$

$$E_{\text{sec}} = \frac{f_{cc}}{\varepsilon_{cc}} \tag{7}$$

where:

k—confinement factor
f_{co}—compressive strength of unconfined concrete
f_{cc}—compressive strength of confined concrete
ε_{co}—strain at maximum concrete stress f_{co}
ε_{cc}—strain at maximum concrete stress f_{cc}
E_c—initial tangent modulus of elasticity and
E_{sec}—secant modulus of elasticity at peak stress of the confined concrete

The tangent modulus of elasticity at any point of the loading branch is given by differentiating Equation (1) with respect to the strain ε_c. Thus,

$$E_{\tan} = \frac{\mathrm{d}f_c}{\mathrm{d}\varepsilon_c} = \frac{(x^r - 1) \cdot f_{cc} \cdot (1 - r) \cdot r}{\varepsilon_{cc} \cdot (x^r + r - 1)^2} \tag{8}$$

When the direction of the imposed load reverses, the loading branch is followed by an unloading branch that starts from point (ε_{un}, f_{un}) (see Figure 1) and is described by a second-order polynomial equation connecting points (ε_{un}, f_{un}) and (ε_{pl}, 0). The latter point lies on the horizontal axis ε_c. The plastic strain ε_{pl} is calculated from the following equations as a function of the unloading strain, ε_{un}. Three different concrete strain regions are used to define ε_{pl}, reflecting the cumulative damage achieved in the element level.

Thus, the following three equations correspond to low, intermediate and high plastic strain range, respectively:

$$\varepsilon_{pl} = \varepsilon_{un} - \frac{f_{un}}{E_c} \ , \ 0 \le \varepsilon_{un} \le \varepsilon_{35} \tag{9}$$

$$\varepsilon_{pl} = \varepsilon_{un} - \frac{\varepsilon_{un} + \varepsilon_a}{f_{un} + E_c \varepsilon_a} \ , \ \varepsilon_{35} \le \varepsilon_{un} \le 2.5\varepsilon_{cc} \tag{10}$$

$$\varepsilon_{pl} = \frac{f_{cr}\varepsilon_{un} - \left|\varepsilon_f\right| f_{un}}{f_{cr} + f_{un}} \ , \ 2.5\varepsilon_{cc} \le \varepsilon_{un} \tag{11}$$

In these equations, strain ε_{35} corresponds to a stress equal to $0.35f_c$, while strains ε_a and ε_f are computed as follows:

$$\varepsilon_a = a\sqrt{\varepsilon_{un}\varepsilon_{cc}} \tag{12}$$

$$a = \max\left[\frac{\varepsilon_{cc}}{\varepsilon_{cc} + \varepsilon_{un}}, \frac{0.09\varepsilon_{un}}{\varepsilon_{cc}}\right] \tag{13}$$

$$\left|\varepsilon_f\right| = \frac{f_{cr}\varepsilon_{plcr}}{E_c\left(\varepsilon_{cr} - \varepsilon_{plcr}\right) - f_{cr}} \tag{14}$$

Term ε_{plcr} is the inelastic plastic strain computed from Equations (9)–(11), using for unloading strain the value $\varepsilon_{un} = \varepsilon_{cr} = 2.5{\cdot}\varepsilon_{cc}$ for confined concrete and the value $\varepsilon_{un} = \varepsilon_{cr} = 2.5{\cdot}\varepsilon_{co}$ for unconfined. Having determined the value of ε_{pl}, the stress and the corresponding tangent modulus of elasticity at any point of the unloading branch are computed as follows:

$$f_c = f_{un}\left(\frac{\varepsilon_c - \varepsilon_{pl}}{\varepsilon_{un} - \varepsilon_{pl}}\right)^2 \tag{15}$$

$$E_{\tan} = \frac{\mathrm{d}f_c}{\mathrm{d}\varepsilon_c} = 2f_{un}\frac{(\varepsilon_c - \varepsilon_{pl})}{(\varepsilon_{un} - \varepsilon_{pl})^2} \tag{16}$$

Finally, the total reloading branch consists of two consecutive and linear segments, each having a different slope.

As depicted in Figure 1, the first reloading segment connects the load reversal point, which may lie on the ε_c axis or above it, with point $(\varepsilon_{un}, f_{new})$, where ε_{un} is the maximum strain ever experienced during the previous loading history. So, for the first reloading segment, strength f_{new} and tangent modulus E_{tan} are computed by the following equations:

$$f_{new} = \frac{f_{cc2} \cdot x \cdot r}{r - 1 + x^r} \tag{17}$$

$$f_{cc2} = 0.9f_{cc} \tag{18}$$

$$x = \frac{\varepsilon_{cc}}{\varepsilon_{cc2}} \tag{19}$$

$$\varepsilon_{cc2} = 0.9\varepsilon_{cc} \tag{20}$$

$$f_c = \frac{f_{ro}(\varepsilon_{un} - \varepsilon_c) + f_{new}(\varepsilon_c - \varepsilon_{ro})}{\varepsilon_{un} - \varepsilon_{ro}} \tag{21}$$

$$E_{\tan} = \frac{\mathrm{d}f_c}{\mathrm{d}\varepsilon_c} = \frac{f_{new} - f_{ro}}{\varepsilon_{new} - \varepsilon_{ro}} \tag{22}$$

In Equations (18) and (19) the values of ε_{co} and f_{co} are used instead of ε_{cc} and f_{cc} for the case of unconfined concrete, i.e., for the cases with concrete under low confinement degree.

The second reloading segment is described with Equation (25). It starts from point $(\varepsilon_{un}, f_{new})$ and ends at the returning point $(\varepsilon_{ret}, f_{ret})$. Strain ε_{ret} and tangent modulus slope E_{tan} for this segment are computed by the following Equations (23) and (26), respectively:

$$\varepsilon_{ret} = \frac{s_r \cdot \varepsilon_{un} + \varepsilon_{un}}{2} \tag{23}$$

$$s_r = 0.00273 + 1.2651 \frac{\varepsilon_{un}}{\varepsilon_{cc}} \tag{24}$$

$$f_c = \frac{f_{new}(\varepsilon_{ret} - \varepsilon_c) + f_{ret}(\varepsilon_c - \varepsilon_{un})}{\varepsilon_{ret} - \varepsilon_{un}} \tag{25}$$

$$E_{\tan} = \frac{\mathrm{d}f_c}{\mathrm{d}\varepsilon_c} = \frac{f_{ret} - f_{new}}{\varepsilon_{ret} - \varepsilon_{un}} \tag{26}$$

In conclusion, a typical complete loading–unloading–reloading cycle of the model of Martinez-Rueda and Elnashai [14], that is implemented in the proposed model and is shown in Figure 3, consists of four branches. One loading branch (red color), one unloading branch (blue color),and two linear consecutive-reloading segments (green and magenta colors). A separate fifth branch (yellow color) is used for tension with zero strength since concrete tensile strength is neglected. This branch follows the blue unloading branch in the case where a tensile loading occurs immediately after unloading.

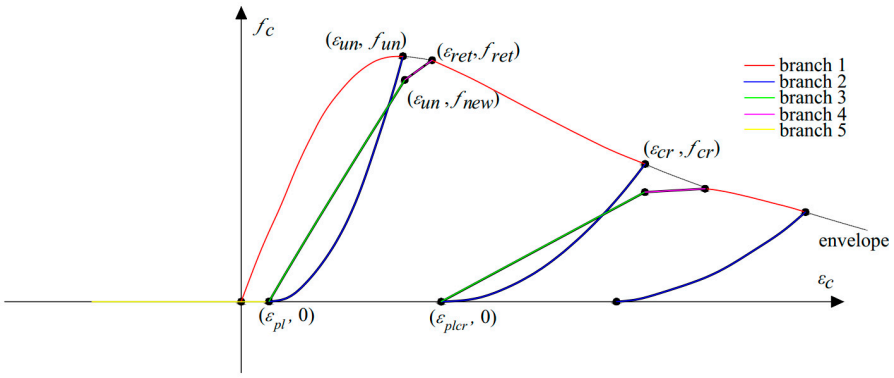

Figure 3. Numbering of branches.

3. Steel Reinforcement Constitutive Stress–Strain Law

The steel constitutive law of Menegotto and Pinto [16] has been incorporated in the proposed model, as it was modified by Filippou et al. [17] and was integrated in Opensees software with the code name Steel02 by Mazzoni et al. [18]. This model is an evolution of the well-known model of Giuffre and Pinto [19], with appropriate modifications in order to better describe the hardening of steel. In Figure 4, a full stress–strain, f_c-ε_c, load cycle is presented (in blue color), as it is obtained from this model, where the various stress and strain parameters are described by Yassin [20].

In this model, load cycles are not composed using discrete branches, as in concrete. Instead, in each loading step the stress–strain response f_s-ε_s is calculated from the following equation set, using normalized values for stress and strain, ${f_s}^*$ and ${\varepsilon_s}^*$, respectively.

$${f_s}^* = b \cdot {\varepsilon_s}^* + \frac{(1-b){\varepsilon_s}^*}{\left[1 + ({\varepsilon_s}^*)^R\right]^{1/R}} \tag{27}$$

$$b = \frac{E_{sh}}{E_o} \text{ (hardening ratio)} \tag{28}$$

$$E_o = \frac{f_o - f_{rev}}{\varepsilon_o - \varepsilon_{rev}} \text{ (tangent modulus of elasticity)} \tag{29}$$

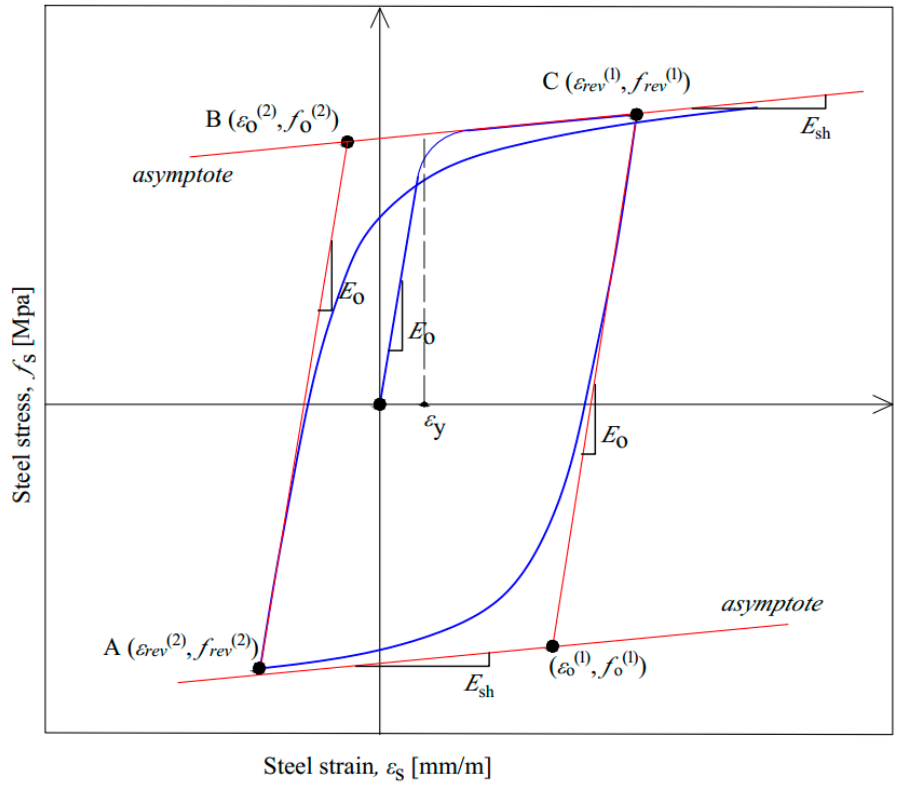

Figure 4. Parameters of Menegotto and Pinto [16] model, according to Yassin [20].

The corresponding normalized values of stress f_s and strain ε_s are defined as follows:

$$f_s{}^* = \frac{f_s - f_{rev}}{f_o - f_{rev}} \tag{30}$$

$$\varepsilon_s{}^* = \frac{\varepsilon_s - \varepsilon_{rev}}{\varepsilon_o - \varepsilon_{rev}} \tag{31}$$

In Equations (29)–(31) (ε_{rev}, f_{rev}) is the last load reversal point, while (ε_o, f_o) is the intersection point between initial and secant stiffness. More specifically, Equation (27) describes a curve with initial tangent stiffness:

$$E_o = f_s{}^* / \varepsilon_s{}^* \tag{32}$$

According to experimental data, for strains where $\varepsilon_s^* \to \infty$ the curve described by Equation (27) asymptotically tends to the following straight-envelope line with slope E_{sh}:

$$f_s{}^* = b \cdot \varepsilon_s{}^* + (1 - b) \tag{33}$$

In the above formulation of Equations (27)–(31), if $\varepsilon_{rev} = f_{rev} = 0$, then the Equation (27) describes pure monotonic loading.

Moreover, if $b = 0$, then the response is elastic–perfectly plastic, while for positive or negative values of b, the post-elastic branch is upward or downward, respectively.

In Figure 4, the superscript of parameters ε_{rev} and f_{rev} denotes the serial number of each subsequent loading. For example, for the first positive loading the superscript is equal to 1, while for the subsequent negative loading the superscript is equal to 2.

Tangent stiffness, E^*_{tan}, results from differentiating Equation (27) with respect to ${\varepsilon_s}^*$ as follows:

$$E^*_{\tan} = \frac{\mathrm{d}{f_s}^*}{\mathrm{d}{\varepsilon_s}^*} = b + \frac{1-b}{\left[1+\left({\varepsilon_s}^*\right)^R\right]^{1/R}} \cdot \left[1 - \frac{\left({\varepsilon_s}^*\right)^R}{1+\left({\varepsilon_s}^*\right)^R}\right] \tag{34}$$

The tangent stiffness, E^*_{tan} of Equation (34), is used in the calculation of the section stiffness along with the corresponding Equation (8) for concrete.

Parameter R is crucial for the behavior of the model and governs the curvature of the loading or unloading branch enclosed between the line with stiffness E_o and that with stiffness E_{sh}. The value of this parameter is adjusted after each load reversal and depends on the value of the maximum plastic excursion, ξ, up to the current loading step:

$$R(\xi) = R_o\left(1 - \frac{cR_1 \cdot \xi}{cR_2 + \xi}\right) \tag{35}$$

$$\xi = \left|\frac{\varepsilon^m - \varepsilon_o}{\varepsilon_y}\right| \tag{36}$$

In the previous equations, $R(\xi)$ is the value of parameter R, after its update according to Equation (35), while R_o is its initial value (see Figure 5). Furthermore, ε^m (where m is an index) is the strain in the previous minimum or maximum (algebraically) load reversal point, depending on whether the deformation increases or decreases, respectively. Thus, referring to Figure 5, which is the stress–strain normalized version of Figure 4, for positive loading $\varepsilon^m = {\varepsilon^1}_{rev}$ (point C in Figure 4) and for negative loading $\varepsilon^m = {\varepsilon^2}_{rev}$ (point A in Figure 4).

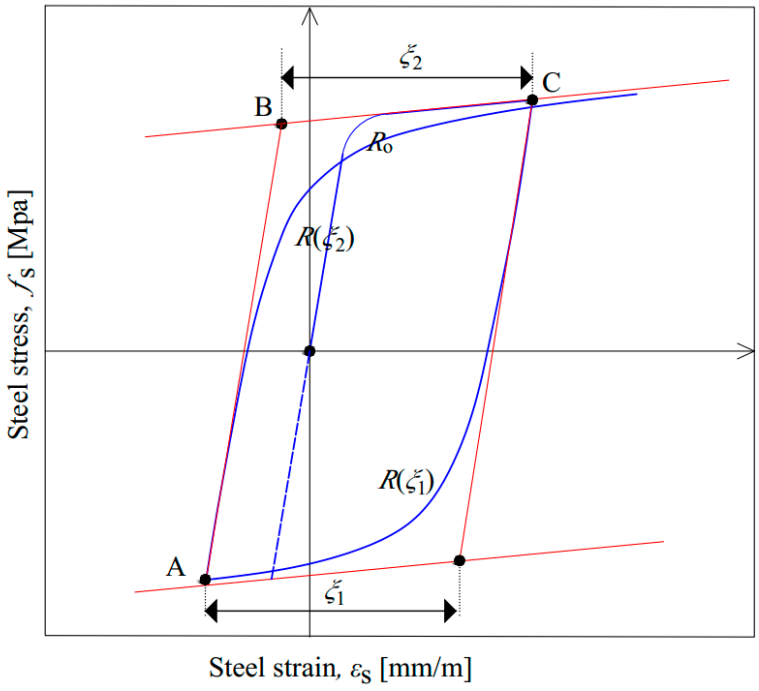

Figure 5. Parameter R in Menegotto and Pinto [16] model, according to Yassin [20].

From the above information, it can be concluded that the calculation of parameter R from Equation (35) requires knowledge of the following parameters of the loading history:

- The value of stress f_s and strain ε_s of the previous loading step.
- The value of stress f_{rev} and strain ε_{rev} of the previous load reversal point, according to Figure 4.

- The value of stress f_o and strain ε_o of the last intersection point between the two branches with stiffnesses E_o and E_{sh}, respectively (see Figure 4).
- The minimum and maximum values of the strain ε_s throughout the loading, ε_{min} and $\varepsilon_{max,}$ respectively.

The steel model is taking into consideration the strain-hardening phenomenon via the modification of ε_o and σ_o according to the following conditions.

When the strain increment $\Delta\varepsilon$ from a positive value becomes negative, then:

$$\Delta^N = 1 + \mathrm{A}_1 \cdot \left(\frac{\varepsilon_{max} - \varepsilon_{min}}{2A_2 \cdot \varepsilon_y} \right)^{0.8} \tag{37}$$

$$\varepsilon_o = \frac{-f_y \cdot \Delta^N + E_{sh} \cdot \varepsilon_y \cdot \Delta^N - f_{rev} + E_0 \cdot \varepsilon_{rev}}{E_0 - E_{sh}} \tag{38}$$

$$\sigma_o = -f_y \cdot \Delta^N + E_{sh} \left(\varepsilon_o + \varepsilon_y \cdot \Delta^N \right) \tag{39}$$

When the stain increment $\Delta\varepsilon$ from a negative value becomes positive, then:

$$\Delta^P = 1 + \mathrm{A}_3 \cdot \left(\frac{\varepsilon^{max} - \varepsilon^{\min}}{2A_4 \varepsilon_y} \right)^{0.8} \tag{40}$$

$$\varepsilon_o = \frac{f_y \cdot \Delta^P - E_{sh} \cdot \varepsilon_y \cdot \Delta^P - f_{rev} + E_0 \cdot \varepsilon_{rev}}{E_0 - E_{sh}} \tag{41}$$

$$\sigma_o = -f_y \cdot \Delta^P + E_{sh} \left(\varepsilon_o + \varepsilon_y \cdot \Delta^P \right) \tag{42}$$

where ε_{max} is the absolute value of the maximum strain in the current loading branch, and ε_y and f_y are the yield strain and yield stress, respectively.

In conclusion, this steel model is capable of capturing the stress hardening during a cyclic loading. The model parameters A_1 to A_4, cR_1, cR_2, and R_o depend on the steel type and can be considered as constant mechanical properties of steel, which are usually determined experimentally. For common steel types used in daily practice, these model parameters that mainly characterize the constitutive law of steel can take the following values in Table 1.

Table 1. Parameter values of steel constitutive model.

Parameter	Proposed Value
b	0.02
R_o	10 to 20
cR_1	0.925
cR_2	0.15
A_1	0.00
A_2	1.00
A_3	0.00
A_4	1.00

4. General RC-Beam-Type Element—FEM Formulation

In this paragraph, the prerequisite mathematical relations for the FEM formulation of the proposed model's algorithm are presented. The model algorithm is described in the next paragraphs.

Figure 6 shows the forces, $\overline{\mathbf{Q}}$, and the corresponding displacement degrees of freedom, $\overline{\mathbf{q}}$, of the member's end nodes in its local coordinate system xyz, considering rigid body mode (RBM). The torsional moment is neglected as it is considered constant and uncoupled with the rest of the degrees of freedom. Thus, the degrees of freedom of each element

consist of three forces and two bending moments corresponding to three displacements and two rotations per end node, respectively.

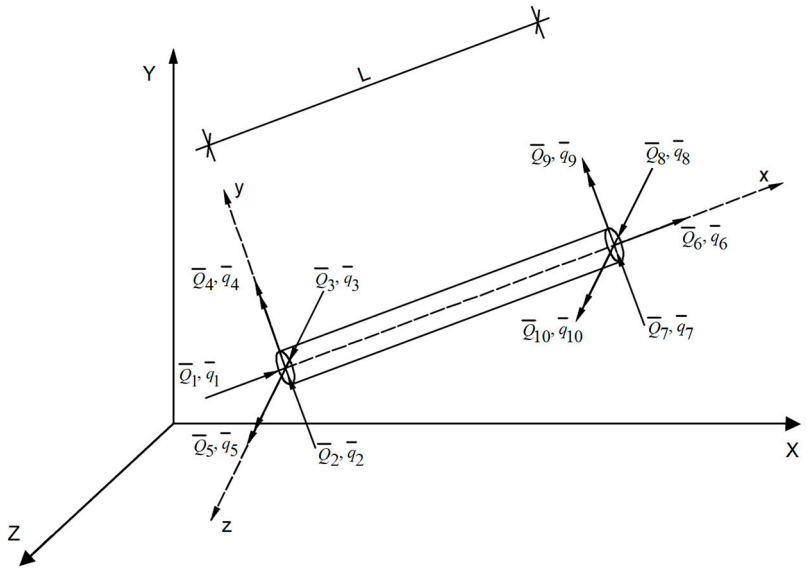

Figure 6. Forces and displacements at element's end nodes considering RBM in the local coordinate system *xyz* (Taucer et al. [5]).

In the present mathematical formulation, in addition to the complete kinematic state, the relative position of the member in the *XYZ* space is also adopted due to its transverse displacements. This relative position results from eliminating the transverse degrees of freedom to the axis of the element. The complete kinematic state can be recovered later based on the geometric relationship that relates the two states. Thus, there are five degrees of freedom left in the member, which correspond to the axial force Q_5 and two bending moments at each node (Q_1, Q_3, and Q_2, Q_4, respectively), as shown in Figure 7. These forces correspond to an axial displacement q_5 and to two rotations per end node (q_1, q_3, and q_2, q_4, respectively).

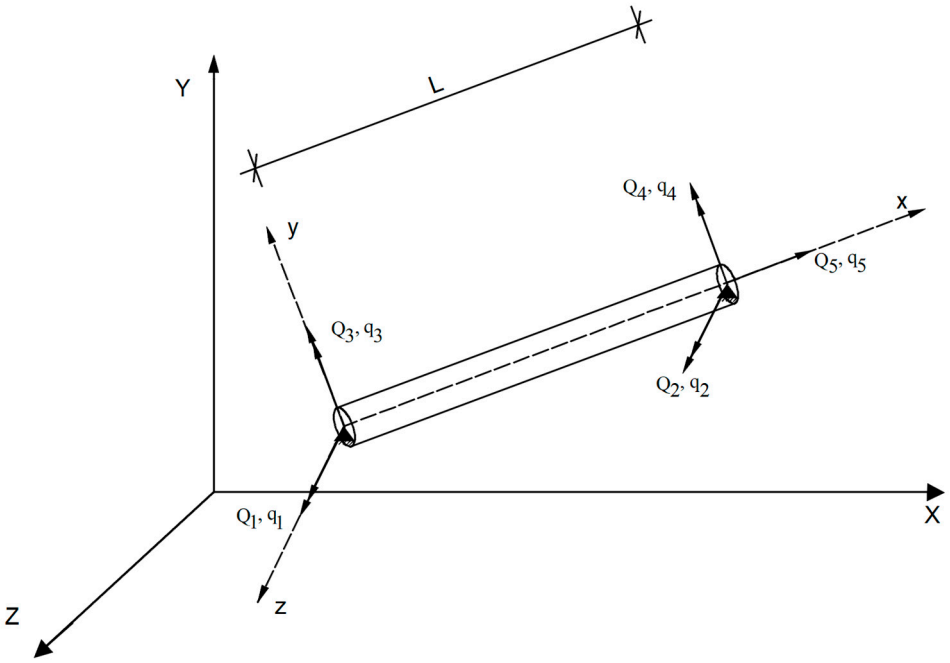

Figure 7. Forces and displacements at the element's ends without considering RBM (Taucer et al. [5]).

Element displacement and force vectors, $\overline{\mathbf{q}}$ and $\overline{\mathbf{Q}}$, (considering RBM) are related to their corresponding vectors, $\mathbf{q}$ and $\mathbf{Q}$, (without RBM) via the following transformation matrix $\mathbf{L}_{RBM}$:

$$\begin{array}{l} \overline{\mathbf{Q}} = \left[\begin{array}{ccccc:ccccc} \overline{Q}_1 & Q_2 & \overline{Q}_3 & \overline{Q}_4 & \overline{Q}_5 & \overline{Q}_6 & \overline{Q}_7 & \overline{Q}_8 & \overline{Q}_9 & \overline{Q}_{10} \end{array} \right]^T \\ \overline{\mathbf{q}} = \left[\begin{array}{ccccc:ccccc} \overline{q}_1 & \overline{q}_2 & \overline{q}_3 & \overline{q}_4 & \overline{q}_5 & \overline{q}_6 & \overline{q}_7 & \overline{q}_8 & \overline{q}_9 & \overline{q}_{10} \end{array} \right]^T \end{array} \tag{43}$$

$$\begin{array}{l} \mathbf{Q} = \left[\begin{array}{ccccc} Q_1 & Q_2 & Q_3 & Q_4 & Q_5 \end{array} \right]^T \\ \mathbf{q} = \left[\begin{array}{ccccc} q_1 & q_2 & q_3 & q_4 & q_5 \end{array} \right]^T \end{array} \tag{44}$$

$$\begin{array}{c} \mathbf{q} = \mathbf{L}_{RBM} \cdot \overline{\mathbf{q}} \\ \mathbf{Q} = \mathbf{L}_{RBM} \cdot \overline{\mathbf{Q}} \end{array} \tag{45}$$

$$\mathbf{L}_{RBM} = \begin{array}{c} \begin{array}{ccccc:ccccc} \bar{1} & \bar{2} & \bar{3} & \bar{4} & \bar{5} & \bar{6} & \bar{7} & \bar{8} & \bar{9} & \overline{10} \end{array} \\ \left[\begin{array}{ccccc:ccccc} 0 & 1/L & 0 & 0 & 1 & 0 & -1/L & 0 & 0 & 0 \\ 0 & 1/L & 0 & 0 & 0 & 0 & -1/L & 0 & 0 & 1 \\ 0 & 0 & -1/L & 1 & 0 & 0 & 0 & 1/L & 0 & 0 \\ 0 & 0 & -1/L & 0 & 0 & 0 & 0 & 1/L & 1 & 0 \\ -1 & 0 & 0 & 0 & 0 & 1 & 0 & 0 & 0 & 0 \end{array} \right] \end{array} \begin{array}{c} \\ 1 \\ 2 \\ 3 \\ 4 \\ 5 \end{array} \tag{46}$$

The conversion of vector quantities (forces, displacements) between local and global coordinate systems is performed through the transformation matrix $\mathbf{L}_{TM}$. In its general form for a finite element with six degrees of freedom per node, the matrix $\mathbf{L}_{TM}$ has the following form,

$$\mathbf{L}_{TM} = \begin{bmatrix} \mathbf{R} & \mathbf{0} & \mathbf{0} & \mathbf{0} \\ \mathbf{0} & \mathbf{R} & \mathbf{0} & \mathbf{0} \\ \mathbf{0} & \mathbf{0} & \mathbf{R} & \mathbf{0} \\ \mathbf{0} & \mathbf{0} & \mathbf{0} & \mathbf{R} \end{bmatrix}, \tag{47}$$

where $\mathbf{R}$ is the following submatrix with the direction cosines C_x, C_y, and C_z with respect to the global coordinate system XYZ. Angle α is the rotation angle around x axis of the element.

$$\mathbf{R} = \begin{bmatrix} C_x & C_y & C_z \\ -\frac{C_x C_y \cos a + C_z \sin a}{C_{xz}} & C_{xz} \cos a & \frac{-C_y C_z \cos a + C_x \sin a}{C_{xz}} \\ \frac{C_x C_y \sin a - C_z \cos a}{C_{xz}} & -C_{xz} \sin a & \frac{C_y C_z \sin a + C_x \cos a}{C_{xz}} \end{bmatrix}, \quad C_{xz} = \sqrt{{C_x}^2 + {C_z}^2} \tag{48}$$

For the present 5-degree-of-freedom element, the 4th and 10th rows and columns of matrix $\mathbf{L}_{TM}$ must be omitted.

Finally, the multiplication $\mathbf{L}_{RBM} \cdot \mathbf{L}_{TM}$ gives the final element-transformation matrix $\mathbf{L}_{ELE}$ that relates the two element states (with and without RBM) and is used for either forces or displacements.

$$\begin{array}{c} \mathbf{L}_{ELE} = \mathbf{L}_{RBM} \cdot \mathbf{L}_{TM} \\ \mathbf{q} = \mathbf{L}_{ELE} \cdot \overline{\mathbf{q}} \\ \mathbf{Q} = \mathbf{L}_{ELE} \cdot \overline{\mathbf{Q}} \end{array} \tag{49}$$

Figure 8 depicts the forces (axial force N and two bending-moment components M_y and M_z with respect to local axes y and z) for a typical cross-section of arbitrary shape of an RC beam element in a distance x from the start node. The corresponding cross-sectional deformations are the axial displacement $\varepsilon_o(x)$ of its mass center cm and the curvature $\varphi(x)$ about the neutral axis n-n with curvature components $\varphi_y(x)$ and $\varphi_z(x)$, respectively. The orientation of axis n-n is $\theta_n(x)$ with respect to the y centroidal axis at a normal distance $d_n(x)$ from point cm.

Thus, without RBM, the force and displacement vectors of the element are:

$$\text{the force vector } \mathbf{Q} = \begin{bmatrix} Q_1 & Q_2 & Q_3 & Q_4 & Q_5 \end{bmatrix}^{\mathbf{T}} \tag{50}$$

$$\text{and the displacement vector } \mathbf{q} = \begin{bmatrix} q_1 & q_2 & q_3 & q_4 & q_5 \end{bmatrix}^{\mathbf{T}} \tag{51}$$

while the corresponding cross-sectional vectors are:

$$\text{the force vector } \mathbf{D}(x) = \begin{bmatrix} M_z(x) \\ M_y(x) \\ N(x) \end{bmatrix} \tag{52}$$

$$\text{and the displacement vector } \mathbf{d}(x) = \begin{bmatrix} \varphi_z(x) \\ \varphi_y(x) \\ \varepsilon_o(x) \end{bmatrix}. \tag{53}$$

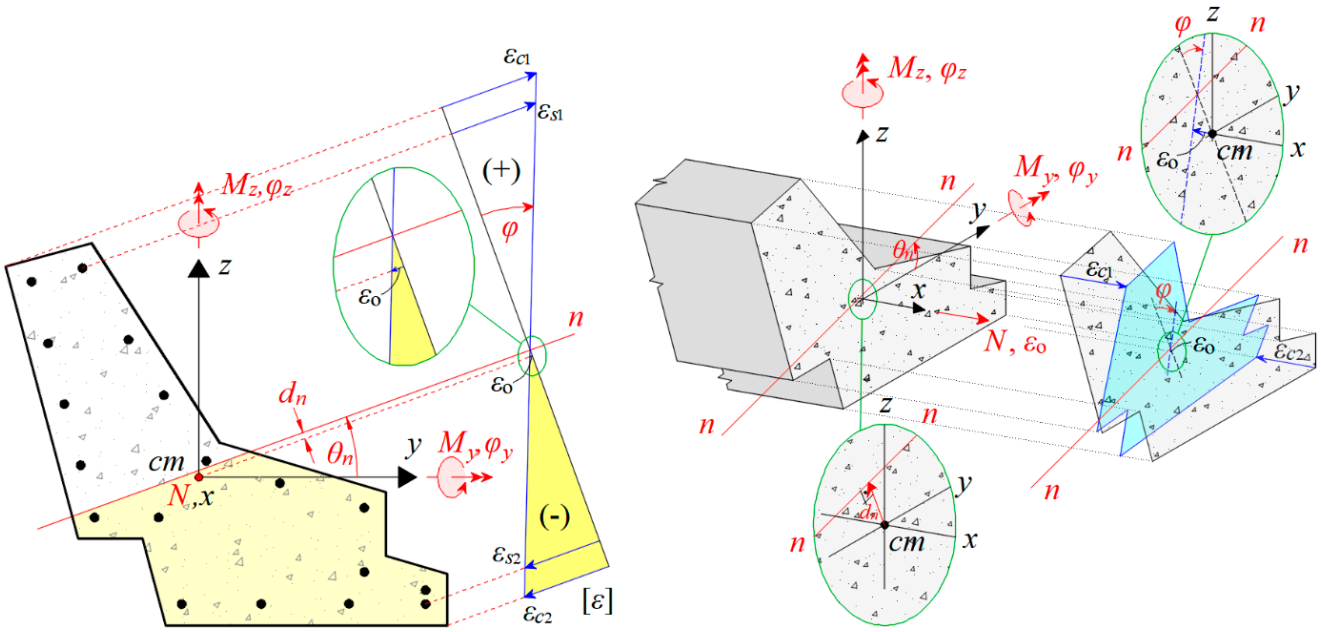

Figure 8. Section forces and deformations.

According to the classic FEM formulation, matrix $\mathbf{b}(x)$ relates the element-nodal load vector $\mathbf{Q}$ with the corresponding cross-sectional load vector $\mathbf{D}(x)$ at a specific location x, using the relation

$$\mathbf{D}(x) = \mathbf{b}(x) \cdot \mathbf{Q} \tag{54}$$

where

$$\mathbf{b}(x) = \begin{matrix} \\ \\ \\ \end{matrix} \begin{matrix} Q_1 & Q_2 & Q_3 & Q_4 & Q_5 \end{matrix} \begin{matrix} \\ \\ \\ \end{matrix} \begin{bmatrix} \frac{x}{L} - 1 & \frac{x}{L} & 0 & 0 & 0 \\ 0 & 0 & \frac{x}{L} - 1 & \frac{x}{L} & 0 \\ 0 & 0 & 0 & 0 & 1 \end{bmatrix} \begin{matrix} M_z(x) \\ M_z(x) \\ N(x) \end{matrix}. \tag{55}$$

In the above equation, it is assumed that the axial force, $N(x)$, remains constant along the length of the member, while the distributions of the bending moments $M_z(x)$ and $M_y(x)$ are linear. Therefore, the interpolation functions described in matrix $\mathbf{b}(x)$ do not cover the case of intermediate loads on a member. To be able to support this case, it is necessary to appropriately modify the interpolation functions of this matrix.

5. Cross-Section Model Based on Polygonal Discretization

The main cross-section-analysis problem of a typical RC member subjected to a known set of bending moments combined with axial force is to find the correct position and orientation of the neutral axis of the cross-section and of its curvature, adopting the classical Navier–Bernoulli assumption about plain sections after bending.

In these geometric computations, calculation of the concrete-compressive force is involved, which is performed by integrating the concrete compressive-stress distribution (usually a second-order polynomial) that acts on a random geometric shape of the compressive zone of the cross-section.

In classical fiber models, the cross-section is divided into fibers, which are usually square, rectangular, or in some cases, triangular. Each fiber is associated with a material, which is either concrete or steel, with the appropriate stress–strain constitutive law, considering only its uniaxial response. The control point of each fiber, i.e., the geometric point at which the stresses are calculated according to the relevant constitutive law, is defined at its mass center. The circular reinforcing bars are placed in their predetermined positions, and their control points are placed at their geometric center.

An example of discretization of a cross-section with random shape into rectangular or square fibers is shown in Figure 9a,b.

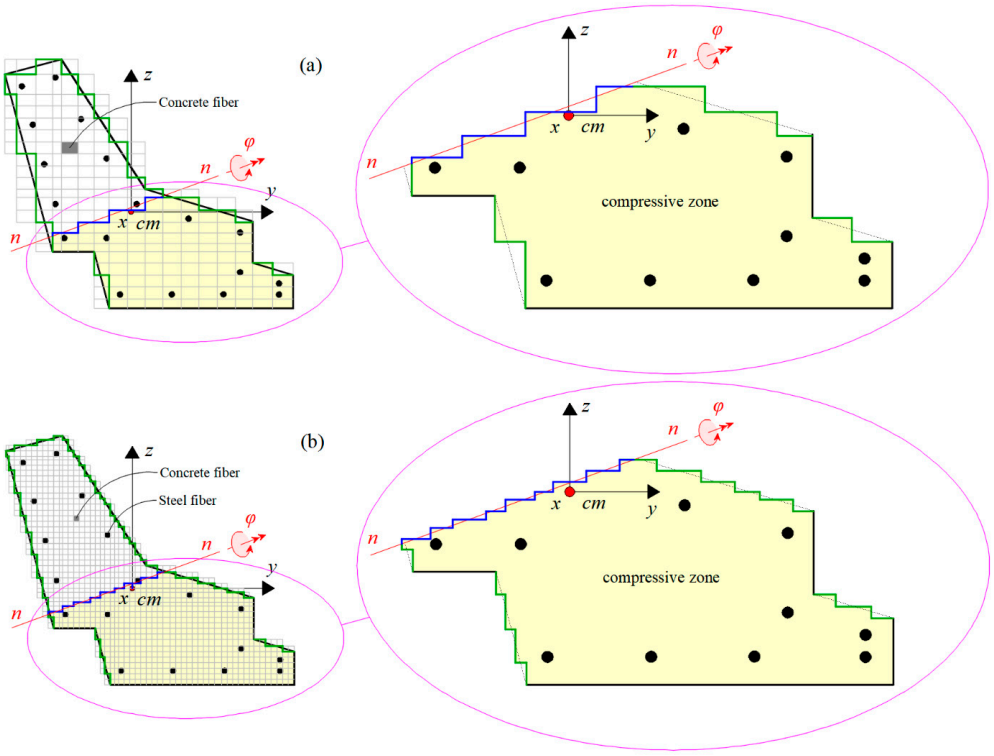

Figure 9. Approximation of cross-section boundaries based on discretization with the classical fiber method. (**a**) mesh of coarse fibers, (**b**) mesh of fine fibers.

Figure 9a shows a coarse-fiber mesh, in which the reinforcement bars are not inscribed in the predefined fibers, which are initially characterized as concrete fibers only. For this reason, the compressive force $F_{s,\text{bar}}$ of a particular steel bar of area $A_{s,\text{bar}}$ and centroid strain $\varepsilon_{s,\text{bar}}$ is computed as

$$F_{s,\text{bar}} = A_{s,\text{bar}} \cdot [\sigma_s(\varepsilon_{s,\text{bar}}) - \sigma_c(\varepsilon_{s,\text{bar}})] \tag{56}$$

where σ_s and σ_c are the stress functions of steel and concrete, respectively.

Figure 9b shows a fine mesh of fibers, with fully inscribed reinforcement bars in the predefined fibers. Thus, the fiber mesh consists of discrete concrete or steel fibers.

In both of the meshes above, a basic computational problem of a geometric nature arises from the use of the classical fiber model, as described above, which in turn can lead to a loss of accuracy in subsequent calculations. The problem is related to the geometrical shape of the fibers (mainly rectangular) that can lead to a loss of computational accuracy when the cross-section edges and/or the neutral axis, *n*-*n*, are not parallel to the local y and z coordinate axes.

In this case, any inclined line (edge or neutral axis) is approximated in a "scalable" form, as shown in Figure 9. Thus, in cases where an inclined line intersects a fiber, the latter is considered to be belonging entirely to the cross-section (for an edge) or in its compressive or tensile part (for the neutral axis), depending on which side of the line its geometric center lies on, as illustrated in Figure 9a,b. For the special case of finding the exact location of an inclined neutral axis, this control leads to enormous convergence problems of the iterative process of searching for this location, especially when this axis is at finite normal distances from the fiber centers. This happens because of the different fiber areas from each side of the inclined neutral axis in combination with their different strains and consequently stresses.

For the classical fiber method, it is known that the accurate computation of the neutral axis position governs in turn the accuracy of the computation of the cross-section's internal force magnitudes. This accuracy and the iterative stability of the algorithm depend on the density of the fiber mesh.

The finer the mesh, the more accurate the results received. On the other hand, a large or huge number of fibers leads to high computational costs, which until recently was a computation barrier for the practical use of fiber computational models to nonlinear analyses of 3D framed structures.

The proposed model aims to give almost identical computational accuracy, solving all of the above computational problems of the classical fiber models. It uses a different approach for the cross-sectional discretization and for the concrete compressive-stress integration over the compressive zone.

The discretization of the cross-section initially concerns its polygonization and subsequently concerns the use of the derived polygons for the purposes of the above-mentioned stress integration. The whole process is performed in the following two stages.

- In the first stage, the cross-section geometric polygonization is performed separately for its cover and its core area. Practically, this means that each one of these two areas is suitably divided into trapezoids or triangles with their bases parallel to one centroidal axis, e.g., *y*. This polygonization process uses the very fast algorithm of Zalik and Clapworthy [21], which can handle any polygonal areas of random geometry, excluding any internal parts (such as holes in the case of RC cross-sections). An example of discretizing such random polygonal areas into trapezoids or triangles is shown in Figure 10, where each different color represents a separate area.

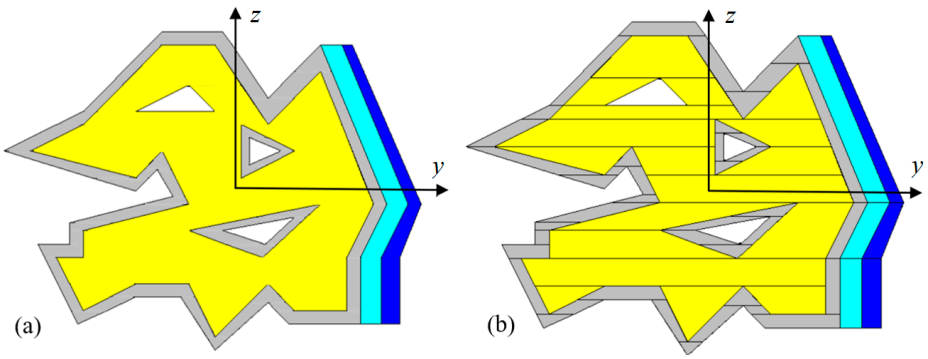

Figure 10. Discretization example of random polygonal geometric areas. (**a**) Original area, (**b**) Discretized area.

- In the second stage of the process, control points are placed uniformly and with appropriate density on the perimeter and the inside of each trapezoid or triangle in order to create a grid of points to be used for Delaunay triangulation. Next, a Voronoi diagram is computed that defines the influence area of each control point. Figure 11 depicts the process of polygonising a random RC-cross-section shape, placing control points in it followed by Delaunay triangulation, and the final result of the Voronoi diagram of each separate polygonal area. Cyan and yellow colors refer to core and cover of the cross-section, respectively.

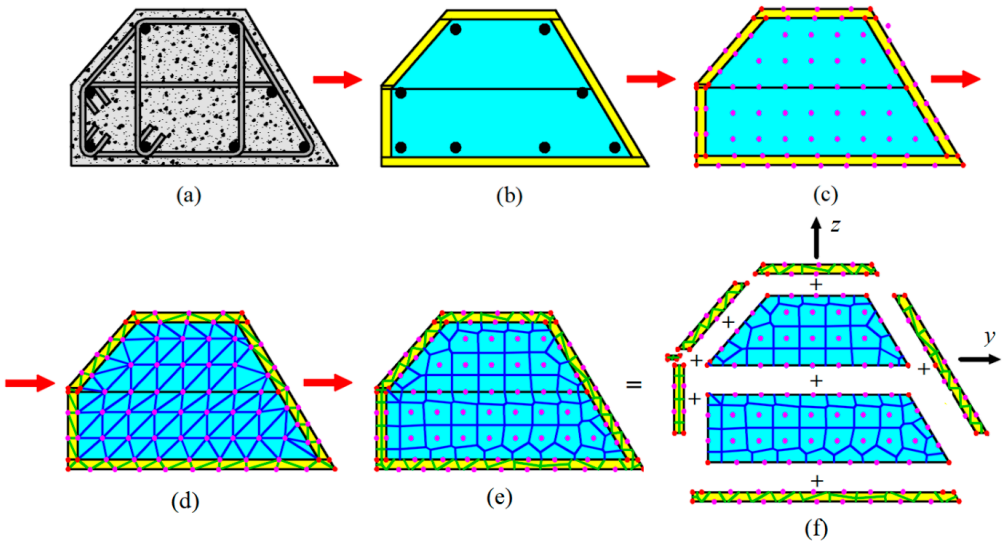

Figure 11. Discretization steps of an RC cross-section: (**a**) cross-section, (**b**) polygonization (trapezoids and rectangles), (**c**) control points, (**d**) Delaunay triangulation, (**e**) Voronoi diagrams per polygonal area, and (**f**) final result.

As will be described in the following sections, the Delaunay triangulation will be used for calculating the concrete-compressive force F_c, due to the distribution of the concrete-compressive stresses over the cross-section compressive area, while the Voronoi diagrams will be used for the computation of the cross-sectional stiffness.

The above-mentioned inelastic constitutive stress–strain law is assigned to control points of a specific trapezoid of a material (concrete cover or confined core). Therefore, the inelastic response at each control point is calculated in each iteration of the main model algorithm, according to its constitutive law.

However, in order to calculate the stiffness of the cross-section, it is also necessary to know the influence area of each control point, *cp*,*i*. This influence area, $A_{Ip,i}$, is obtained from the calculated Voronoi diagram of all the points of each trapezoid (Figures 11e,f and 12).

Following the classic definition of the Voronoi diagram (Figure 12), it should be recalled that for a given plain area with a given set of scattered points in it, which are considered control points, the diagram is essentially a discretization of the whole area into a set of individual influence areas, one for each control point of the set. A unique characteristic of a particular influence area is that all of the points contained within it are closer to its particular control point than to any other point of the given control-point set. Thus, each Voronoi area can be considered the influence area of its control point.

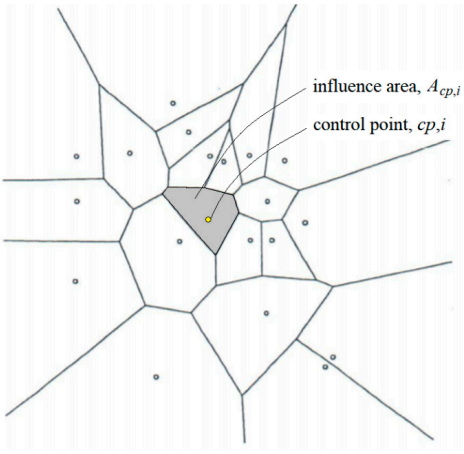

Figure 12. Example of a Voronoi diagram for a given dataset of control points with their corresponding influence areas.

5.1. Control Cross-Sections and Neutral Axis Position and Orientation

The main algorithm of the proposed model, which is described in the following section, considers a number of control cross-sections along its axial coordinate x (Figure 13) in order to take into account the distributed inelasticity over its length L.

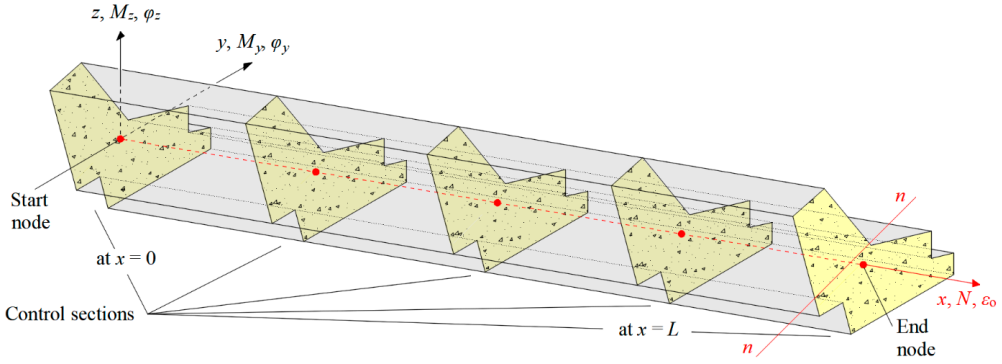

Figure 13. Control cross-sections along element length and neutral axis *n*-*n*.

For each load step, the deformation vector $\mathbf{d}(x)$ of Equation (53) of each control cross-section is computed iteratively in the global algorithm of the model. Thus, for a specific control section, the values of the components ε_o, φ_y, and φ_z of vector $\mathbf{d}(x)$ determine the position and orientation of the neutral axis *n*-*n*. After that, the internal axial load N and its corresponding moment components M_y and M_z, of the force vector $\mathbf{D}(x)$ of Equation (52) can be computed, adopting the aforementioned triangulation technique. The computation of N, M_y, and M_z is performed per material, concrete or steel, as described in the following text.

5.2. Concrete Compressive Resultant Force F_c

In the proposed model, for every neutral axis position and orientation in a particular control cross-section, the process of calculating the concrete-resultant-compressive force F_c over the compressive zone of this cross-section significantly differs from that followed in the classical fiber models. In the proposed model, the 3D shell shape of concrete-compressive stresses σ_c is obtained point-by-point from the determination of the corresponding stresses at each vertex (control point) of the Delaunay triangles. Thus, the total resultant compressive force F_c of concrete is calculated as the volume enclosed by this 3D shell.

The general case of a cross-section under bending with combined axial load considers two parts of the total compressive zone of a cross-section: the unconfined part, consisting of the concrete cover, and the confined one, consisting of the concrete core inside the stirrups. Each of these parts obeys its own 3D shell of concrete-compressive stresses due to the different strengths of these two concrete parts. The subcase where the two parts obey a unique continuous 3D shell of stresses is that in which the confinement by the stirrups is extremely small and is thus neglected. This happens in old RC structures with insufficient stirrup confinement.

Figure 14 shows the 3D-shell shape of concrete-compressive stresses σ_c for the random cross-section shape of Figures 8 and 9. For presentation simplicity, insufficient stirrup confinement is assumed so both the concrete cover and the core of the compressive zone are affected by a continuous 3D shell of stresses. Due to biaxial bending conditions, an inclined neutral axis *n*-*n* is shown, at angle θ_n with respect to the centroidal axis y. It is noted that angle θ_n differs in general from the angle a of the bending moment components M_y and M_z of the external imposed-bending moment vector M, as explained in Sfakianakis [22]. A typical triangle with vertices as the control points, *cp*,*i*, is shown in the compression zone of the cross-section, in correspondence with Figure 11d, as resulted from the polygonization technique.

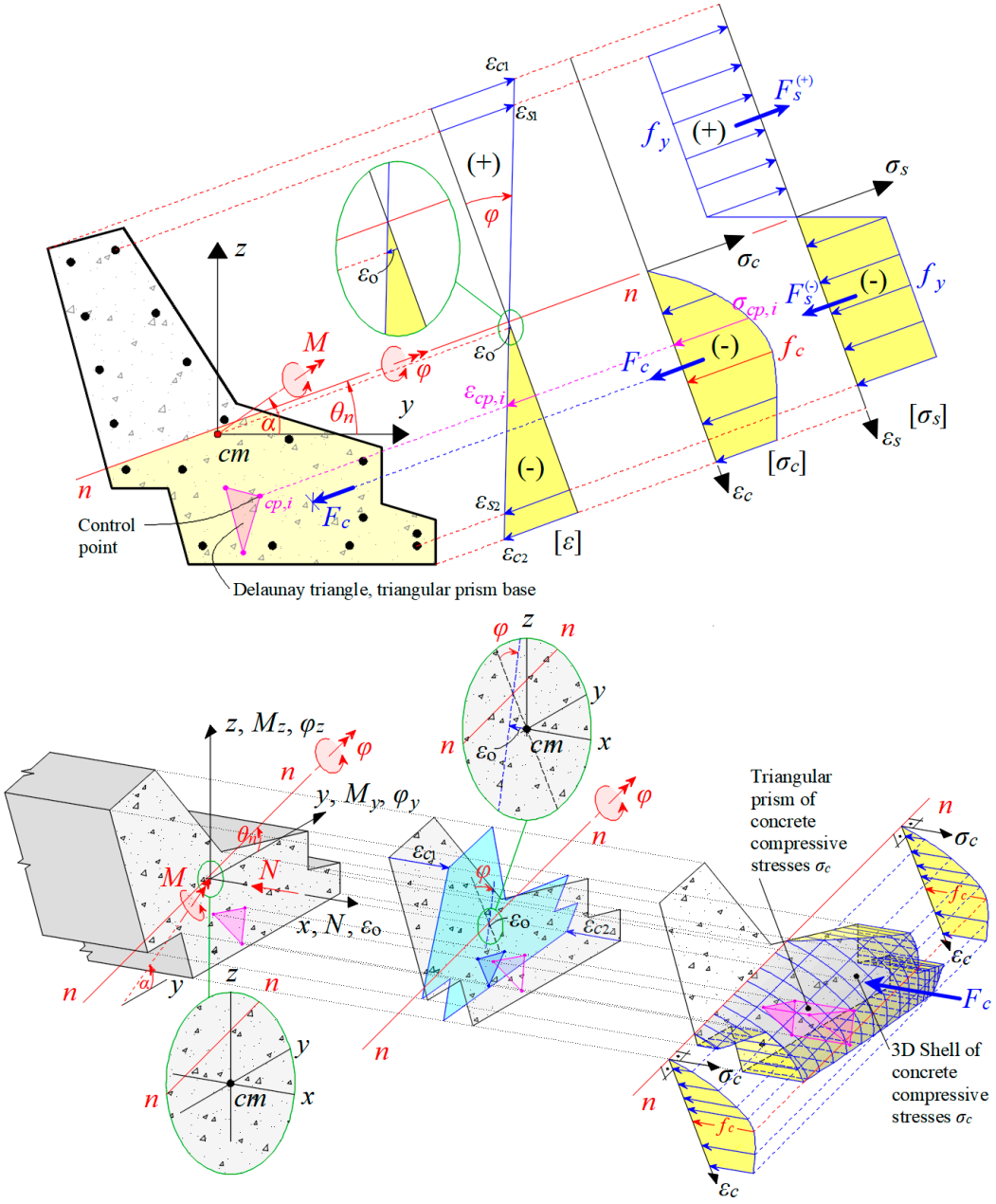

Figure 14. 3D shell of concrete compressive stresses under biaxial bending conditions combined with compressive axial load.

Each vertex *cp,i* has a strain $I_{cp,i}$ and a concrete-compressive stress $\sigma_{cp,i}$. Adopting the Navier–Bernoulli assumption about plain cross-sections after bending, the strain $\varepsilon_{cp,i}$ is computed as

$$\varepsilon_{cp,i}(y_{cp,i}, z_{cp,i}) = \varepsilon_o - y_{cp,i} \cdot \varphi_z + z_{cp,i} \cdot \varphi_y \quad (57)$$

whereas the concrete-compressive stress $\sigma_{cp,i}(\varepsilon_{cp,i})$ is computed from the constitutive stress–strain law of Section 2.

Thus, the shape of the 3D shell of the concrete-compressive stresses is approximated by drawing the values of the stresses $\sigma_c = \sigma_{cp,i}$ of each control point $c_{p,i}$ of the cross-section, corresponding to a given deformation $\varepsilon_c = \varepsilon_{cp,i}$ that is calculated using Equation (57). As a result, the 3D shell of the stress space is composed of triangular prisms. The bases of these triangular prisms, on the cross-section plane, correspond to the Delaunay triangulation, while their tops form the 3D shell of the concrete-compressive stresses on the compression zone of the cross-section. An example of the formed 3D stress surface is given in

Figure 15a for a classic rectangular cross-section, considering biaxial bending (inclined neutral axis *n*-*n*) and an unconfined concrete core. Figure 15b shows the detail of Delaunay triangles intersected by the neutral axis *n*-*n*. Each of these triangles, and their corresponding triangular prisms, is split into a compressive part (yellow color) and a tensile part (cyan color), the latter with zero stress values.

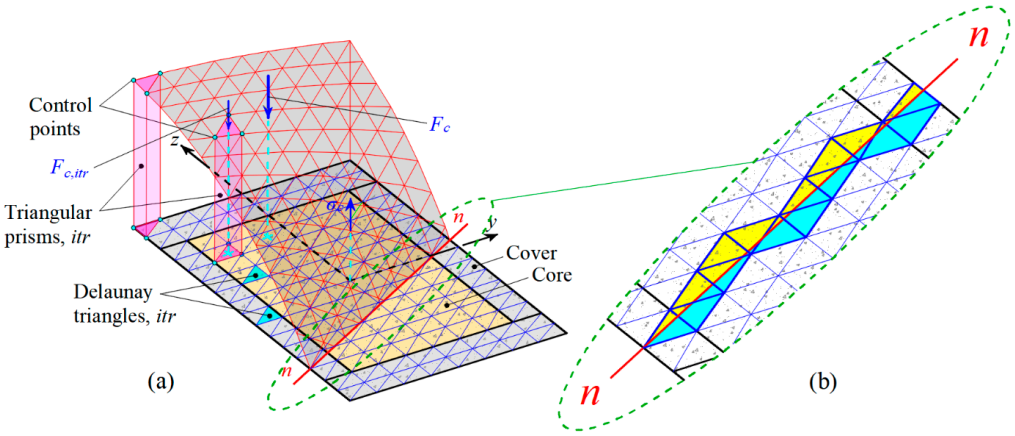

Figure 15. 3D shell of concrete-compressive stresses σ_c and neutral axis *n*-*n*. (**a**) Triangulation process and (**b**) Delaunay triangles intersected by the neutral axis.

Because of this splitting, each triangular prism is divided into two different stereometric shapes (i.e., tetrahedron, etc.).

The special case where, during previous load steps, a failure has been preceded in one or two compressed vertices of a split triangle by the neutral axis is taken into account by setting zeroed values for the compressive stresses in these vertices. The same technique is also applied to concrete vertices that are entirely inside the compressive zone of the cross-section where a failure may had occurred during previous load steps.

Figure 16 shows all of the six possible stereometric forms of the prisms, which may occur according to the following scenarios:

- Cut of a prism by a plane normal to the cross-section plane and passing through the neutral axis *n*-*n*, considering failure or no failure of the vertices.
- A prism belonging entirely to the compressive zone with one or more vertices in failure during previous load steps.

Stresses $\sigma_{1,2,3}$ are the concrete-compressive stresses of vertices 1, 2, and 3 of a Delaunay triangle. Force $F_{c,tr}$ is the resultant compressive force of the remaining compressed stereometric part of the triangular prism, after it is cut off, while (y_{tr}, z_{tr}) are the coordinates of the point of application of this force. The cyan-shaded areas denote the cut-off part of the triangle with completely zeroed stresses. Flowchart FC4 in Appendix A shows the searching algorithm for categorizing a prism to one of the six stereometric cases of Figure 16, based on the stress state of its triangular base.

In this way, the progressive failure of small concrete areas inside the compressive zone is also taken into account quite realistically. To achieve this result, the previous loading history of each control point $c_{p,i}$ must be taken into account. For the cross-section of Figure 15, Figure 17 shows an indicative "subsidence" that occurs in the 3D shell of concrete compressive stresses σ_c due to the failure of two control points.

Finally, for the computation of the resultant concrete (index "*con*") compressive force F_c, only the n nonzero prismatic volumes inside the compressive zone of a particular control cross-section are taken into account. This force and its moment components M_y and M_z are computed as follows:

$$N^{con} = F_c = \sum_{itr=1}^{n} F_{itr}\ ,\ M_y^{con} = \sum_{itr=1}^{n} F_{itr} \cdot z_{itr}\ ,\ M_z^{con} = \sum_{itr=1}^{n} F_{itr} \cdot y_{itr} \tag{58}$$

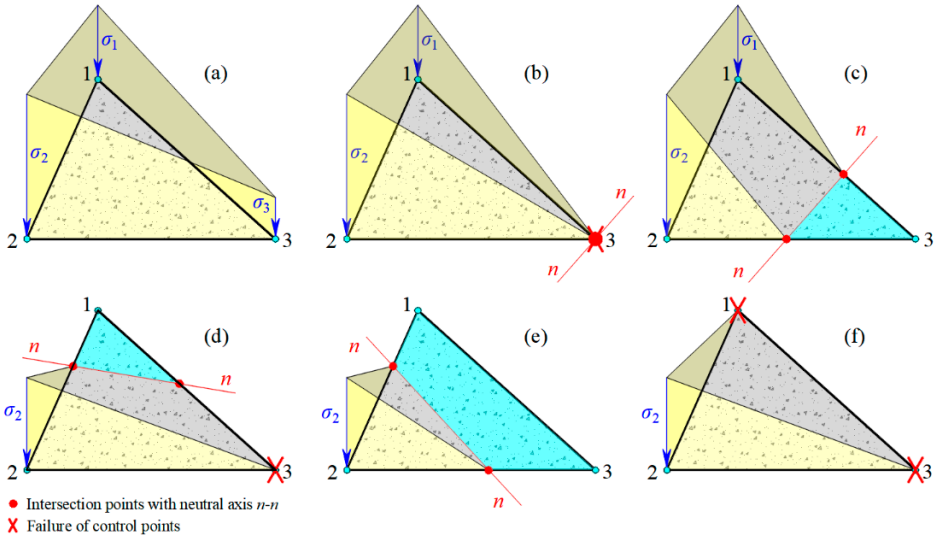

Figure 16. (**a**–**f**) show all the possible stereometric forms of triangular prisms after their intersection with the neutral axis *n*-*n* or failure of control points.

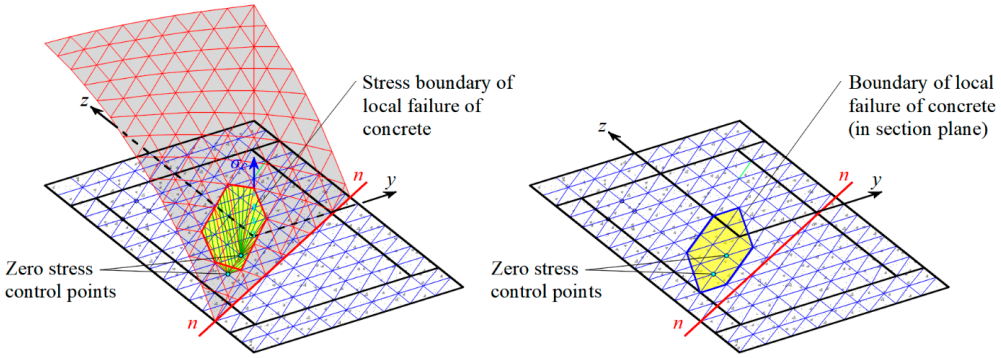

Figure 17. 3D shell of concrete-compressive stresses σ_c considering local failure of concrete.

5.3. Steel Resultant Force Fs

For the calculation of the resultant force F_s of the longitudinal-reinforcement steel bars, the constitutive law of Section 3 is used. For each bar, *ibar*, with section area $A_{iba}r$ and position coordinates (y_{ibar}, z_{ibar}) in the cross-section, its stress σ_{ibar} is computed as a function of its centroidal strain ε_{ibar}. The latter is computed from Equation (58) after replacing subscript *cp*,*i* with *ibar*. Thus, the resultant steel (index "*st*") force F_s and its moment components M_y and M_z in a particular control cross-section are computed as follows:

$$N^{st} = F_s = \sum_{ibar=1}^{nbar} \sigma_{ibar} \cdot A_{ibar}\,,\; M_y^{st} = \sum_{ibar=1}^{nbar} \sigma_{ibar} \cdot A_{ibar} \cdot z_{ibar}\,,\; M_z^{st} = \sum_{ibar=1}^{nbar} \sigma_{ibar} \cdot A_{ibar} \cdot y_{ibar} \tag{59}$$

For a more accurate calculation of the internal force and moment components of the cross-section, the circular areas A_{ibar} that are occupied by the steel-reinforcing bars must be subtracted from the surface of the Delaunay triangles. The methodology implemented to achieve this is the placement of additional control points for the concrete-steel bar regions, *icbar*, at the centroids of the reinforcing bars, having assigned on them the constitutive law of concrete. In this way, the resultant concrete-steel (index "*cst*") force and its moment components at regions A_{ibar}, which must be subtracted, are computed as follows:

$$N^{cst} = \sum_{ibar=1}^{nbar} \sigma_{icbar} \cdot A_{ibar}\,,\; M_y^{cst} = \sum_{ibar=1}^{nbar} \sigma_{icbar} \cdot A_{ibar} \cdot z_{ibar}\,,\; M_z^{cst} = \sum_{ibar=1}^{nbar} \sigma_{icbar} \cdot A_{ibar} \cdot y_{ibar} \tag{60}$$

5.4. Final Internal Force and Moment of Cross-Section

For each control cross-section of coordinate x along the element length (Figure 13), the final internal axial load N and its moment components M_y and M_z are obtained as the algebraic sum of the Equations (58)–(60).

$$N = N^{con} + N^{st} - N^{cst}\ ,\ M_y = M_y^{con} + M_y^{st} - M_y^{cst}\ ,\ M_z = M_z^{con} + M_z^{st} - M_z^{cst} \tag{61}$$

5.5. Cross-Section Stiffness Matrix

In the FEM formulation of the proposed model, the stiffness matrices $\mathbf{k}_s$ of the control cross-sections are used for the derivation of the element-stiffness matrix $\mathbf{K}_E$. For each control cross-section with coordinate x along the element length, its stiffness matrix $\mathbf{k}_s$ is formulated as the contributions of all of the n Voronoi regions of area $A_{cp,i}$ of the control points cp,i with coordinates ($y_{cp,i}$, $z_{cp,i}$) (Figures 11f and 12). Taucer et al. [5] used the same formulation for their fiber model, where the areas $A_{cp,i}$ were those of the fibers. The modulus of elasticity $E_{cp,i}$ of each control point is computed from Equations (8), (16), (22) and (25), depending on the loading-unloading-reloading branch of the concrete constitutive law in which its stress–strain state belongs. Following these definitions, the relation of the cross-sectional stiffness matrix $\mathbf{k}_s$ is as follows:

$$\mathbf{k}_S = \begin{array}{c} \begin{matrix} \quad M_z \quad & \quad M_y \quad & \quad N \quad \end{matrix} \\ \left[\begin{array}{c|c|c} \sum_{cp,i=1}^{n} E_{cp,i} \cdot A_{cp,i} \cdot y_{cp,i}^2 & \sum_{cp,i=1}^{n} E_{cp,i} \cdot A_{cp,i} \cdot y_{cp,i} \cdot z_{cp,i} & \sum_{cp,i=1}^{n} E_{cp,i} \cdot A_{cp,i} \cdot y_{cp,i} \\ \hline \sum_{cp,i=1}^{n} E_{cp,i} \cdot A_{cp,i} \cdot y_{cp,i} \cdot z_{cp,i} & \sum_{cp,i=1}^{n} E_{cp,i} \cdot A_{cp,i} \cdot z_{cp,i}^2 & \sum_{cp,i=1}^{n} E_{cp,i} \cdot A_{cp,i} \cdot z_{cp,i} \\ \hline \sum_{cp,i=1}^{n} E_{cp,i} \cdot A_{cp,i} \cdot y_{cp,i} & \sum_{cp,i=1}^{n} E_{cp,i} \cdot A_{cp,i} \cdot z_{cp,i} & \sum_{cp,i=1}^{n} E_{cp,i} \cdot A_{cp,i} \end{array}\right] \begin{matrix} \varphi_z \\ \varphi_y \\ N \end{matrix} \end{array} \tag{62}$$

6. Algorithm of the Proposed Model

In the following sections, the critical points of the algorithm of the proposed model are described at the levels of structure, member, and cross-section. The complete algorithm is provided in three flowchart forms in Appendix A, and it is presented with full computational detailing for each of its steps. It consists of the following three nested iterative loops:

- The first-outer loop (Flowchart FC1) refers to the classic FEM formulation on the structural level, introducing some major modifications for the needs of convergence, as will be described in Section 6.1.
- The second loop (Flowchart FC2), internal to FC1, refers to the element level. The mixed-formulation method of Taucer et al. [5] is applied for equilibrium achievement for each element of the structure, using an iterative procedure.
- Finally, the third loop (Flowchart FC3), internal to FC2, refers to the cross-sectional level of an element. The cross-section equilibrium is achieved through an iterative process, based on the element's nodal internal forces and displacements of the second loop (Flowchart FC2). This process is applied to each cross-section of the element as a subroutine of the second loop. For reference purposes, the computational steps of each flowchart of Appendix A are accompanied with numbering.

6.1. Algorithm of the Proposed Model on the Structural Level

As mentioned before, the mixed-formulation method of Taucer et al. [5] is the basis of the developed FE algorithm on the structural level. The choice was made using the criterion that this algorithm outperforms in comparison with other alternative ones in terms of the numerical stability it provides. More specifically, according to this reference, the major advantages of the algorithm can be summarized as follows:

- Equilibrium is always satisfied throughout an RC member after selecting linear interpolation functions assuming no intermediate loads on the member. Compatibility of deformations is achieved by computing the member's end deformations by integrating those of the distributed control cross-sections.
- The inelastic response of the RC members can be calculated without particular computational difficulties, even in cases of lightly reinforced members or members under high axial load.

Special convergence criteria and methods for avoiding numerical problems have been introduced in the main FE algorithm (Flowchart FC1), which are critical for the proposed model. Numerical problems can arise for a number of reasons, the main ones being the following:

- The use of the Newton–Raphson method, whose convergence becomes unstable when the tangent stiffness tends to zero.
- The advanced degree of inelasticity of the structure. This can happen when a number of control cross-sections of elements have yielded or failed.
- The partial failure of cross-sections, caused either by concrete cracking or by yielding of the reinforcement bars.
- The method of calculating the cross-section's internal forces (more details in Section 6.2)
- Imposing large values of load increments.
- Accumulative error, regarding the unbalanced forces, from previous analysis steps.

The main and critical points of the FEM algorithm are described in the next sections, in reference to flowchart FC1 of Appendix A.

6.1.1. Loop for the Application of Load Steps

The outermost loop, with backward step order 15-16-17-18-19-20-6 (red path), refers to the imposing of load-step increments $\Delta\mathbf{P}$ in the structural level. In this loop, the load-step counter is denoted as k, while the iteration counter within a load step (intermediate loop) is denoted as i. The loop is repeated for every step k of the analysis. The load is imposed in the form of load increments $\Delta\mathbf{P}$, considering all structural degrees of freedom.

At every load step k and iteration i, solution for the change of the displacement increments $\delta\Delta\mathbf{U}^{k,i}$ is performed in step 7. With given $\delta\Delta\mathbf{U}^{k,i}$, the element-state determination is computed in step 9. Then, the loop continues with the classic FE formulation in steps 12 through 15. In step 15, the convergence of the algorithm is checked. If it is successful, then all of the necessary quantities are updated in step 16 (i.e., element and structure stiffness, forces and deformations of element control cross-sections and stress–strain status of control points cp) following the classic FE formulation.

6.1.2. Convergence Criteria for Newton–Raphson Iterations per Load Step

The intermediate loop, with backward step order 15-22-23-24-7 (green path), refers to the iterations of the Newton–Raphson method, which is necessary for the determination of the structure state in terms of forces and deformations at each load step. These iterations, indicated by i, aim for the minimization of the unbalanced forces of the structure, resulting in convergence of the algorithm and therefore the equilibrium of the structure.

The decision for convergence or no convergence is made in step 15, which includes two criteria for this purpose. Convergence is considered to be achieved if at least one of the two criteria is satisfied.

The first criterion is the major one and it concerns the evolution of the relative change of the structure internal forces $\mathbf{P}_{int}$ in successive iterations i of the following algorithm

$$\left| \frac{\mathbf{P}_{int}^{i} - \mathbf{P}_{int}^{i-1}}{\mathbf{P}_{int}^{i-1}} \right| < tol1 \tag{63}$$

where the tolerance $tol1$ usually takes values between 0.001 and 0.01. The criterion is applied for each degree of freedom of the structure.

The second convergence criterion accompanies the first and concerns the decreasing evolution of the absolute values of the unbalanced forces, according to the equation

$$\left|\mathbf{P}_U^i\right| < tol2 \tag{64}$$

where *tol2* depends on the number of iterations *i* in the structure level of the algorithm.

It is also applied for each degree of freedom of the structure and is checked along with the first criterion in each iteration *i*, if necessary. Generally, the value of tolerance *tol*2 gradually relaxes the value of limit *tol*1, but in terms of load values (forces or moments), up to an upper limit predefined by the user for the computer analysis.

As it is explained in detail in a section below, in the case of no convergence at all, for a particular load step *k*, the load increment $\Delta\mathbf{P}$ is reduced by successive divisions by three and computations of the load step *k* are repeated from the beginning. The greater number of successive divisions of the load increment declares the greater difficulty of the algorithm to converge. The small increase of the value of *tol2* leads to a "relaxation" of this convergence criterion. But it is pointed out that this relaxation facilitates convergence at the current load step *k*, while at the same time it has no adverse effect on the overall accuracy. The small error introduced in the current load step *k* is corrected in the next *k* + 1, where the tolerance *tol2* is reset to its original value. Thus, the minimal negative influence of the second accompanying convergence criterion is locally limited to the specific step in which the problem occurred.

The combination of the above two convergence criteria guarantees the stability and convergence of the overall FE algorithm as it has been successfully verified in a large number of analyses for predicting experimental results.

6.1.3. Loop for Calculation of Unbalanced Forces per Element

The innermost loop, with backward step order 10-11-9 (blue path), refers to the application of the mixed-formulation method to determine the force and deformation state of each element of the structure. For this purpose, step 9 of this loop is implemented in the embedded flowchart FC2 and it is presented in Section 6.2. In this inner flowchart, convergence is considered to be achieved after *j* iterations trying to minimize the unbalanced forces of the element.

6.1.4. Split of the load-step increment for Convergence of the FEM Algorithm

The most usual numerical problems that occur in the practical application of similar FEM formulations and lead the algorithm to no convergence for equilibrium, are the following:

- The iterations of the algorithm do not lead to the solution monotonically.
- The algorithm is getting "trapped" between two values, one on each side of the solution ("flip-flop" phenomenon).
- Unacceptable convergence tolerance.

In the proposed model, a simple methodology for handling such problems has been introduced to the main FEM algorithm. It is based on the fact that small loading steps $\Delta\mathbf{P}$ usually lead to easier convergence. As for the computational cost due to the possible use of many small steps, this is discussed in Section 7.

Thus, for convergence purposes, a maximum number of Newton–Raphson iterations, *max_iter*, is defined in which the method is expected to converge without problems. If, in a particular load step *k*, this value is reached without convergence of the algorithm, then the initial load increment $\Delta\mathbf{P}^k$ is divided by 3 and the computational process of load step *k* starts from the beginning (setting the iteration counter *i* to zero), with a "new" $\Delta\mathbf{P}$ value equal to $\Delta\mathbf{P}^k_{1/3} = \Delta\mathbf{P}^k/3$. If the algorithm fails again to converge, having reached the maximum number of iterations *max_iter*, the previous process is repeated by dividing the already reduced value of $\Delta\mathbf{P}^k/3$ by 3. The new value $\Delta\mathbf{P}^k_{1/3} = \Delta\mathbf{P}^k/3^2$ is now used for the recomputation of step *k*. This process of dividing the initial load-step increment $\Delta\mathbf{P}^k$ by

three is continued until a final appropriate value $\Delta\mathbf{P}^k_{1/3} = \frac{\Delta\mathbf{P}^k}{3^{split3}} < \Delta\mathbf{P}^k$ is found for which convergence occurs for load step k. Superscript *split3* is the counter of the number of divisions by 3. Therefore, for *split3* number of successive divisions, the current value of $\Delta\boldsymbol{P}^k_{1/3}$ is given by the following equation:

$$\Delta\mathbf{P}^k_{1/3} = \frac{\Delta\mathbf{P}^k}{3^{split3}} \tag{65}$$

The decision for the splitting of load increment $\Delta\mathbf{P}^k$ is made in step 22 of the algorithm. Split is activated if *i* = *max_iter* and the whole process follows the backward step order 22-25-26-6 of flowchart FC1.

Thus, step k is divided into two parts, the first $\Delta\boldsymbol{P}^k_{1/3}$ and the second $\Delta\boldsymbol{P}^k_{res}$ that is equal to:

$$\Delta\mathbf{P}^k_{res} = \Delta\mathbf{P}^k - \Delta\mathbf{P}^k_{1/3} = \Delta\mathbf{P}^k - \frac{\Delta\mathbf{P}^k}{3^{split3}} \tag{66}$$

If the application of the first part leads to convergence, then the application of the second part follows without changing the load-step counter k, i.e., this second part is applied as a supplementary load portion in the current step k. The process of application of the second part $\Delta\boldsymbol{P}^k_{res}$ is implemented in steps 17-21-6 of flowchart FC1. The decision for this application is made in step 17 that gives a "reminder" that a previous split has occurred in step 22.

As mentioned previously, the two convergence criteria of step 15 are used, when the split-load increments $\Delta\boldsymbol{P}^k_{1/3}$ and $\Delta\boldsymbol{P}^k_{res}$ are applied.

In flowchart FC1, the magenta paths refer to the bifurcation of steps 22 and 17 of the algorithm, when the process of applying a reduced load increment $\Delta\boldsymbol{P}^k_{1/3}$ and its supplementary value $\Delta\boldsymbol{P}^k_{res}$ is activated.

This methodology of local reductions of the loading increments $\Delta\mathbf{P}$, when needed, proved to be very effective. For the purpose of computing cost, in combination with getting only a small error, divisions by three proved to be the best choice after thorough numerical investigation with other values, such as two, four, and five.

6.2. Algorithm of the Proposed Model on the Element Level

In classic FEM formulation, in analysis step-iteration *k*-*i*, the following displacement vector is applied to the structural end nodes of an element:

$$\mathbf{q}^{k,i} = \mathbf{q}^{k-1,i} + \Delta\mathbf{q}^{k,i} \tag{67}$$

As proposed by Taucer et al. [5], internal to iteration i, another iterative procedure (with iteration index j) is taking place with the aim of minimizing the unbalanced forces in the cross-section level.

The procedure starts with the computation of the nodal-force increments $\Delta\mathbf{Q}^j$ of each element in iteration j as

$$\Delta\mathbf{Q}^j = \left[\mathbf{F}_E{}^{j-1}\right]^{-1} \cdot \Delta\mathbf{q}^j = \mathbf{K}_E{}^{j-1} \cdot \Delta\mathbf{q}^j \text{ if } j = 1 \tag{68}$$

Herein, the element's flexibility matrix, $\mathbf{F}_E$, results from integrating the individual flexibility matrices $\mathbf{f}_s(x)$ of the control cross-sections over the element length using the Gauss–Lobato integration scheme as follows:

$$\mathbf{F}_E^{j-1} = \int_0^L \mathbf{b}^{\mathrm{T}}(x) \cdot \mathbf{f}_s^{j-1}(x) \cdot \mathbf{b}(x)dx \Rightarrow \mathbf{K}_E^{j-1} = \left[\mathbf{F}_E^{j-1}\right]^{-1} \tag{69}$$

Thus, the element-stiffness matrix $\mathbf{K}_E$ can be computed by inverting its flexibility matrix $\mathbf{F}_E$.

Next, from the element nodal-force increments $\Delta\mathbf{Q}^j$ the control cross-section force increment vector $\Delta\mathbf{D}^j(x)$ can be derived using Equation (55), i.e.,

$$\Delta\mathbf{D}^j(x) = \mathbf{b}(x) \cdot \Delta\mathbf{Q}^j \tag{70}$$

For each control cross-section x, the corresponding deformation vector $\Delta\mathbf{d}^j(x)$ is computed from the following equation.

$$\Delta\mathbf{d}^j(x) = \mathbf{r}^{j-1}(x) + \mathbf{f}_s^{j-1}(x) \cdot \Delta\mathbf{D}^j(x)\ ,\ x \in [0, L] \tag{71}$$

In Equation (71), $\boldsymbol{f}_s^{j-1}(x)$ is the cross-section-flexibility matrix at the previous iteration $j-1$, and $\boldsymbol{r}^{j-1}(x)$ is the corresponding vector of the residual deformations that must be minimized during the j iterations. This vector was computed in the previous iteration $j-1$, as

$$\mathbf{r}^{j-1}(x) = \mathbf{f}_s^{j-1}(x) \cdot \mathbf{D}_U^{j-1}(x)\ ,\ \mathbf{D}_U^{j-1}(x) = \mathbf{D}^{j-1}(x) - \mathbf{D}_{int}^{j-1}(x) \tag{72}$$

where $\boldsymbol{D}_U^{j-1}(x)$ is the cross-section's unbalanced forces and $\boldsymbol{D}^{j-1}(x)$, $\boldsymbol{D}_{int}^{j-1(x)}$ are its external and internal forces, respectively.

Then, for the current iteration j, the internal cross-section forces $\boldsymbol{D}_{int}^{j(x)}$ are computed. The computation is based on the procedure of Section 5 and is implemented in the embedded flowchart FC3 (see Section 6.3). Also, new values of quantities $\boldsymbol{D}_U^j(x)$ and $\boldsymbol{r}^j(x)$ are computed from Equation (72). The cross-section-flexibility matrix $\boldsymbol{f}_s^j(x)$ is computed by inverting the corresponding stiffness matrix $\boldsymbol{k}_s^j(x)$ of Equation (62).

The execution of the above computations for all control cross-sections of an element is followed by the update of its flexibility and stiffness matrices, $\mathbf{F}_E^j$ and $\mathbf{K}_E^j$, respectively, using Equation (69), for use in the next iteration $j+1$.

The final step of the above procedure is the check for minimization of the unbalanced forces $\boldsymbol{D}_U^j(x)$ for every control cross-section x, using the convergence criteria of Section 6.1. If convergence is not achieved, a new iteration $j+1$ starts with the element's residual displacements $\boldsymbol{s}_E^j$ in place of the original $\Delta\mathbf{q}^j$ of Equation (68). The element's residual displacements are computed by integrating the residual deformations $\boldsymbol{r}^j(x)$ of all control sections over its length using the Gauss–Lobato integration scheme:

$$\mathbf{s}_E^j = \int_0^L \mathbf{b}^{\mathrm{T}}(x) \cdot \mathbf{r}^j(x) dx \tag{73}$$

It is obvious that the formulation method of Taucer et al. [5] is a hybrid method in the sense that it tries to satisfy both the equilibrium conditions and the compatibility of nodal displacements with cross-section deformations.

The above iterative computations of the control cross section incremental force vector $\Delta\mathbf{D}$ and the corresponding deformation vector $\Delta\mathbf{d}$ are similar to that of the Newton–Raphson method in the structural level.

On the element and cross-sectional levels, the mixed-formulation method of Taucer et al. [5] works primarily with the infinitesimal changes $\delta\Delta\mathbf{x}$ of increments $\Delta\mathbf{x}$, with $\mathbf{x}$ being the force or displacement or deformation vectors of an element and of its control cross-sections.

In the following sections, the main and critical points of the algorithm on element level are described with reference to flowchart FC2 of Appendix A.

6.2.1. Loop for Element-state determination

The outermost loop of the algorithm, with backward step order 13-14-15-17-18-2 (red path), refers to each element *ele* of the structure. It encloses the full algorithmic-iterative procedure that was described previously in detail, i.e., all of the computations on the element and cross-sections levels.

Initially, in step 2 the incremental displacement changes $\delta\Delta\underline{\boldsymbol{q}}^{k,i}$ of the ends of each element are recovered from the vector of structural displacements $\Delta\mathbf{U}$, which in turn are converted without RBM mode, i.e., to $\delta\Delta\mathbf{q}^{k,i}$ (see Figures 6 and 7 and Equations (43)–(49)). Then, in step 3 follows the update of the element-end-nodal-displacement increments $\Delta\boldsymbol{q}^{k,i}$. Step 4 and onward follow the iterative procedure of the algorithm.

6.2.2. Loop for Iterations

The intermediate loop, with backward step order 13-19-23-24-5 (green path), encloses the iterative part of the computations, on element and cross section levels, which are performed in each iteration j of the algorithm. A maximum number *max_iter_elem* of permitted iterations is assumed. The decision for convergence of the unbalanced forces $\boldsymbol{D}_U^{k,i,j}$ of the control cross-sections of each element is made in step 13. The two convergence criteria of Section 6.1 are used.

In steps 12 and 23, the Gauss–Lobato integrations of Equations (69) and (72) are performed with weights w. Subscript *sec* denotes positions x of the control cross-sections along an element length.

6.2.3. Loop for Cross-Sections

The innermost loop, with backward step order 10-11-7a (blue path), encloses the computations of the algorithm related to the control cross-sections, *sec*, of each element. The aim of this loop is the computation of the unbalanced forces $\boldsymbol{D}_U^{k,i,j}$ of each control section of an element. This computation is performed in step 8 of this loop and is implemented in the embedded flowchart FC3 which is presented in Section 6.3. Moreover, in this loop the residual deformations $\boldsymbol{r}^{k,i,j}$ the flexibility and stiffness matrices, $\boldsymbol{f}_s^{k,i,j}$ and $\boldsymbol{k}_s^{k,i,j}$, respectively, are computed and stored for each control cross-section of an element.

6.2.4. Split of the Change of the Element Incremental Displacement

In cases where the maximum permitted number of iterations *max_iter_elem* is exceeded without convergence in step 13, a procedure for reducing the order of magnitude of the change of the incremental displacements $\delta\Delta\underline{\boldsymbol{q}}^{k,i}$ is applied, similarly to that for the incremental load step $\Delta\mathbf{P}^k$ in the main FEM algorithm (see Section 6.1).

The reduction of $\delta\Delta\underline{\boldsymbol{q}}^{k,i}$ is achieved by successively dividing its current value by three. A counter *split3e* is used for the number of divisions, establishing an upper bound *max_split3e* for them.

It is to be remembered that these reductions of $\delta\Delta\underline{\boldsymbol{q}}^{k,i}$ occur during the current load step k and iteration i of the FEM algorithm. Thus, in cases where the bound *max_split3e* has been exceeded (step 20) it is assumed that there is no convergence for the current element, and the flow of computations returns to step 25 of flowchart FC1 for new reduction of $\Delta\mathbf{P}^k$. In this way, the algorithm is not "trapped" to unlimited reductions of $\delta\Delta\underline{\boldsymbol{q}}^{k,i}$ for a particular element, thanks to the upper bound *max_split3e*. If convergence is achieved for a reduced value of $\delta\Delta\underline{\boldsymbol{q}}^{k,i}$, $\delta\Delta\underline{\boldsymbol{q}}_{1/3}^{k,i}$, then rest value $\delta\Delta\underline{\boldsymbol{q}}_{res}^{k,i} = \delta\Delta\underline{\boldsymbol{q}}^{k,i} - \delta\Delta\underline{\boldsymbol{q}}_{1/3}^{k,i}$ is applied supplementarily.

In flowchart FC2, the magenta paths refer to the bifurcation of steps 19 and 15 of the algorithm, when the process of applying a reduced load increment $\delta\Delta\underline{\boldsymbol{q}}_{1/3}^{k,i}$ and its supplementary value $\delta\Delta\underline{\boldsymbol{q}}_{res}^{k,i}$ is activated.

If the reduction process is successful, then the flow of computations returns to step 10 of flowchart FC1.

6.3. Algorithm of the Proposed Model on the Cross-Section Level

In this section, the part of the algorithm for computing the internal resisting force vector $\mathbf{D}_{\text{int}}$ of each control section of the element is described. This part is implemented in flowchart FC3 and consists of three independent and successive loops of computations which are described in the following sections.

6.3.1. Loop for Concrete Stresses of Control Points of a Cross-Section

In this loop, the concrete-compressive stress σ_{cp} is computed for each concrete control point, cp, of the total, N_{cp}, of a control cross-section of an element.

Following the assumption of Navier–Bernoulli for plane sections remaining plane after bending, the axial deformation of each control point cp of a cross-section in distance x from the member's start node is computed from Equation (57), i.e.,

$$\varepsilon_{cp}(x, y_{cp}, z_{cp}) = \varepsilon_{\text{o}} + y_{cp} \cdot \varphi_z(x) + z_{cp} \cdot \varphi_y(x)\ , cp = 1, N_{cp} \tag{74}$$

Then, for each control point cp, its stress $\sigma_{cp}(\varepsilon_{cp})$ is computed in step 3 from the concrete σ–ε constitutive law of Section 2. It is to be remembered that this law takes into account the previous loading history of each control point, i.e., in which unloading or reloading branch it belongs.

6.3.2. Loop for Concrete Forces F_c of Triangular Prisms

Having computed in the previous loop the stresses σ_{cp} of the vertices of each Delaunay triangle, tr, of the total Ntr triangles of the concrete cross-section, the corresponding triangular prism's concrete-compressive force $F_{c,tr}$ is now computed, along with the coordinates (y_{tr}, z_{tr}) of the point of its application. These computations take place in step 8, taking into account the subcases of the intersected prisms (see Section 5, Figures 15 and 16) that are included in flowchart FC4.

The total axial force N and its moment components M_y and M_z, which are due to concrete-compressive stresses only, are computed in step 9 (see Equation (58)).

6.3.3. Loop for Rebar Forces

In the third loop, the forces F_b of the reinforcement-longitudinal bars are computed according to Equation (59) for each bar, b, of total N_b. The axial force F_b of a bar is equal to $\sigma_b \cdot A_b$, where σ_b and A_b are the axial stress and area, respectively, in its center point, which is a separate control point for this purpose. Stress σ_b is a function of the bar's axial strain ε_b, $\sigma_b = \sigma_b(\varepsilon_b)$, with ε_b computed in step 13 as

$$\varepsilon_b(x, y_b, z_b) = \varepsilon_{\text{o}} + y_b \cdot \varphi_z(x) + z_b \cdot \varphi_y(x)\ , b = 1, N_b \tag{75}$$

Then, in step 14 the stress $\sigma_b(\varepsilon_b)$ is computed from the steel σ–ε constitutive law of Section 3. As with concrete, the steel σ–ε law takes into account the previous loading history of the bar's center point.

For each bar, in step 15 its axial force F_b and its moment components $M_{y,b}$ and M_{zb} are computed (see Equation (59)), while in step 16 they are added to the total force and moments of the cross-section.

In step 17, force F_{cd} and its moment components $M_{y,cb}$ and $M_{z,cb}$ are computed for the cyclic area of concrete occupied by each reinforcing bar (see Equation (60)). This force and these moments are then subtracted from the corresponding ones of the cross-section in step 18.

Thus, after the completion of the computations of the three loops, the internal resisting force vector $\mathbf{D}_{\text{int}} = [N, M_y, M_z]^{\text{T}}$ of a cross-section has been fully determined and the flow of computations returns to step 8 of flowchart FC2.

7. Significant Computational Characteristics of the Proposed Model

The proposed model aims to give a very good accuracy of its predicted numerical results in comparison with experimental data, provided either in the specimen level or in the form of scaled structures, while keeping the computational cost at a reasonable level.

Extensive previous experience using classical fiber models has shown that their numerical accuracy depends on fine discretization of the fiber grid that leads to high computational cost, even with the use of computational parallelization, in regard to modern computers used in daily practice by engineers. When using a coarse discretization of the fiber grid for keeping a low computational cost, the numerical accuracy gradually falls due to the extremely approximative manner of integrating the concrete-compressive stresses σ_c over the compressive zone of the cross-section. As this computational integration procedure is embedded in the core of the algorithm of most of the inelastic models for RC beam elements, it has been proved that the low accuracy of computation of the concrete compressive resultant force F_c and its acting point leads to an increase in Newton–Raphson iterations and, therefore, in the computational cost (e.g., nonlinear analyses with SAP2000 or ETABS using alternatively coarse or fine fiber discretization). Thus, when focusing on relevant issues, such as:

- the issue of computational accuracy with reference to the aforementioned stress integration and cross-section-stiffness computation,
- the cross-section geometric shapes,
- the computational cost of the model, and
- the convergence improvement of the algorithm,

The basic computational characteristics of the proposed model, which give closer numerical results to the experimental data in comparison with the models of Taucer et al. [5] and Spacone et al. [6–8], are being summarized in the following subsections.

7.1. Shape of 3D Shell of Concrete-Compressive Stresses σ_c—Delaunay Triangularization

For the rectangular cross-section of Figures 15 and 18b shows the "scalable" forms of the 3D-shell surface of stresses and of the neutral axis *n-n*, as produced by a fiber model using a moderate-to-coarse grid of fibers. In classic fiber models, the cross-sections of fibers are usually defined as rectangular, assuming constant stress equal to that of their mass center, which also serves as a control point. The proposed model uses the polygonization technique described in Section 5, according to which the polygons are transformed to a Delaunay grid of triangles, with their vertices serving as stress-control points. Comparison of the results between the proposed model and the fiber model shows the evident superiority of the first, since it leads to the exact representation of the shell surface of concrete-compressive stresses.

7.2. Inclined Cross-Section Boundaries with Respect to the Centroidal Axes

In the case of inclined cross-section boundaries with respect to the centroidal axes, the classic fiber models approach any inclined boundary line in a "scalable" form, as depicted in Figures 9 and 19. Figure 19 shows such an inclined boundary of a cross-section for which unconfined concrete is assumed for both cover and core. Between the proposed model and that of fibers, there is a deviation of the concrete-compressive-stress values in the vicinity of the inclined boundary that is usually a common reason for the losses of accuracy and convergence in the fiber models when they are used with relatively coarse fiber grid.

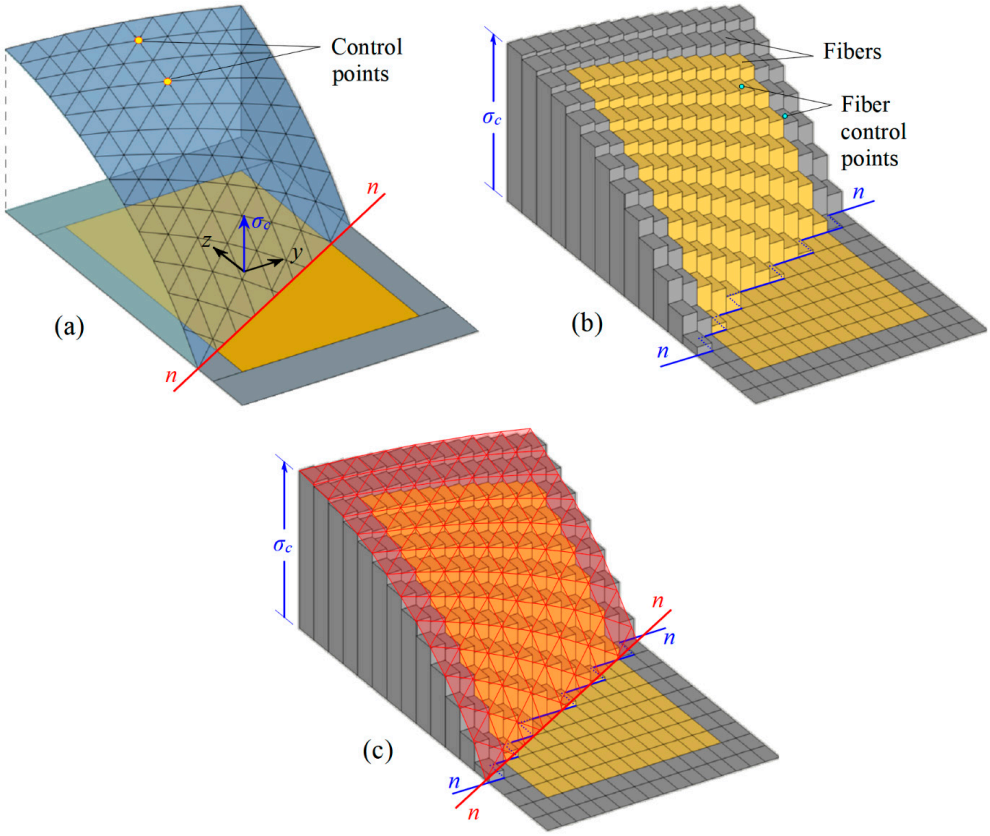

Figure 18. 3D shell shape of concrete-compressive stresses σ_c and neutral axis n-n. (**a**) Proposed model, (**b**) classic fiber model, and (**c**) model's circumscribed stress shell to the "scalable" model of the fibers.

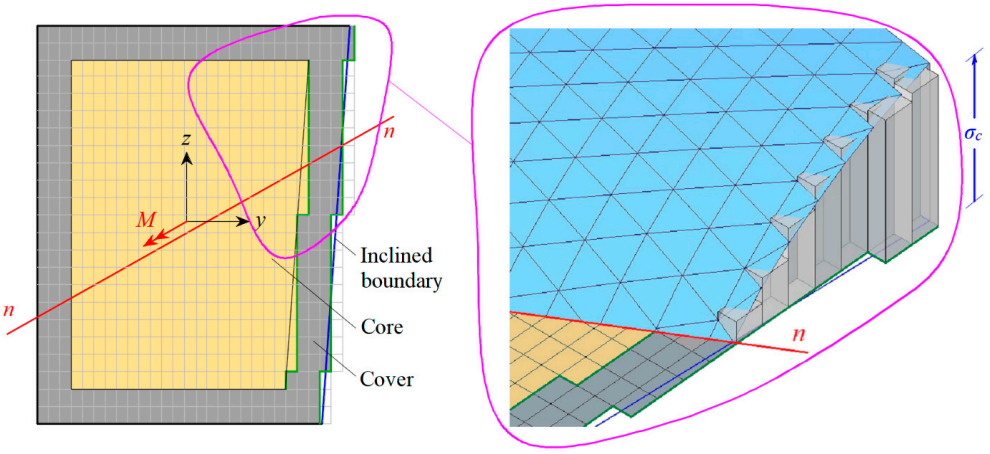

Figure 19. Concrete-compressive-stress approach at cross-section-inclined boundary by the proposed model and the classic fiber model.

7.3. Compressive Stresses σ_c at the Outermost Compressive Boundary of the Cross-Section

Another problem that leads to the loss of accuracy and convergence of the fiber models, with relatively coarse fiber grids, is related to the concrete-compressive-stress values of the outermost compressible boundary of the cross-section. As is shown in Figure 20, in the classic fiber models the concrete-compressive stresses are calculated at the center points of the fibers. These points deviate from the actual boundaries of the cross-section. In contrast, the proposed model uses control points that lie on the real boundaries (see Figure 20). This

means that any abrupt stress fluctuations close to the outermost compressive boundary that may occur, for example due to cyclic loading, are accurately captured.

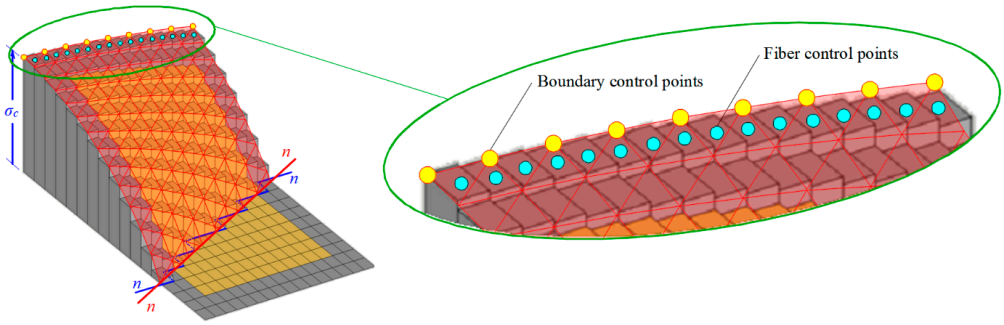

Figure 20. Concrete compressive stresses σ_c at the outermost compressible boundary of cross section. Comparison of proposed and classic fiber model.

7.4. Cross-Section Stiffness Matrix—Voronoi Diagram of Control Points

For the computation of the stiffness matrices of the control cross-sections of an element, a Voronoi diagram of the stress-control points is used. Based on the definition of a Voronoi diagram, the basic idea is that the stiffness of the cross-section area around a particular control point can reliably defined by the Voronoi area of this point. This technique led to rapid convergence of the model's algorithm, significantly reducing the number of iterations per load step, as resulted from thorough numerical investigations on this theme. For this reason, the use of Voronoi diagrams in the topic of the computation of the cross-section stiffness matrix is considered a very important innovation of the present model.

7.5. Search Algorithms for Neutral Axis Position

Numerical algorithms of some RC-beam-element models of distributed inelasticity for use a direct geometrical search algorithm for locating the position and orientation of neutral axis *n-n* of control cross-sections, for given values of end-nodal displacements and forces of an element. In fiber models, mainly when used with a relatively coarse-fiber grid, this search algorithm may fall into a reciprocating "entrapment" within the dimension of the height of a fiber, e.g., in the case of uniaxial bending of an orthogonal cross-section, as depicted in Figure 21. This happens mainly because of the constant stress value over the whole area of the fiber.

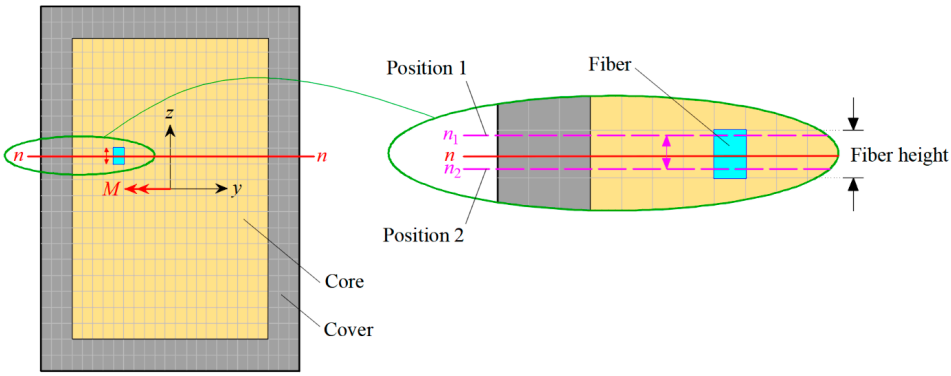

Figure 21. Reciprocating "entrapment" of the neutral axis *n-n* between positions 1 and 2 within the height of a fiber row.

The proposed model does not directly use such a geometrical search algorithm. Instead, the cross-section deformation vector **d**, which describes the position and orientation of the neutral axis *n-n*, results from Equation (71) iteratively (see Section 6.2 and step 7b of flowchart FC2). Taking into account accurately the variation of stress values perpendicularly

to the neutral axis, in combination with the geometric procedures for Delaunay triangles that are intersected by it (see Section 5), the algorithm of the proposed model is free of the danger of such "entrapment".

Of course, the aforementioned iterative procedure of the proposed model could be characterized as an indirect geometrical search of the position and orientation of neutral axis *n-n*.

7.6. Arbitrary Cross-Section Shapes

The main characteristic of the proposed model is that it can handle cross-sections of arbitrary geometric shapes without the loss of accuracy regarding the before mentioned integration over a geometrically randomly shaped compressive zone under biaxial bending conditions combined with axial force.

7.7. Computational Cost of the Proposed Model

Coming to computational cost of the proposed model as a function of the discretization of the cross-section with the Delaunay triangular grid, thorough numerical investigations showed that a relatively coarse grid is enough for the accuracy and the convergence of the algorithm. This is a major advantage of the proposed model in comparison to the requested high discretization of the fiber models. The low computational cost of the proposed model was also checked in a modern computer, similar to those used in daily practice by the engineers.

7.8. Computer Implementation—Convergence Improvement of the Algorithm

The proposed model is implemented in the form of a finite element in the MINOS FEM code, originally developed by Sfakianakis [23] in the university of Patras in Greece. Further modifications were made on the core of the FEM algorithm in order to be adapted to the mixed-formulation method of Taucer et al. [5]. The program is of general purpose and is focused on nonlinear analyses of framed and solid structures with various types of inelastic FE in its library. Verification applications of the proposed model using the MINOS FEM code include the inelastic response prediction of experiments of beam and column specimens and 2D and 3D scaled frames, and these are presented in Part II of this paper.

Focusing on the computational part of the algorithm, another major advantage is the procedure of splitting the structural load increments $\Delta\mathbf{P}$ and/or the incremental displacements $\Delta\mathbf{q}$ at the element level, which has been proven as very efficient for the convergence of the whole algorithm. When needed, this procedure is activated automatically.

7.9. Concrete and Steel Reinforcement Parameters for Nonlinear Analyses

Usually, the incorporation of inelastic cyclic concrete and steel models into the development of corresponding mathematical inelastic beam models for RC members must be followed with the definition of the values of the ultimate strains ε_{cu} and ε_{su} for concrete and steel, respectively. Beyond these values, it is assumed that the complete failure modes of the two materials have taken place.

For the case of nonlinear analysis for the prediction of the experimental nonlinear response of a specimen (i.e., a single RC member or a scaled structure) these values, especially for concrete, must be provided by the experimental investigators. If not, then the most realistic values are those of specific modern codes for interventions, such as Part 3 of the Eurocode 8 or the Greek Code for Interventions and Repairs of RC Structures KAN.EPE. [24].

For the concrete ultimate strain ε_{cu}, the above codes give formulas for both unconfined and confined concrete, covering the most usual cases of the geometric shape of the confined core of a cross-section. The value of the steel-ultimate strain ε_{su} is also given from the above codes, distinguishing this for the cases of before and after spalling of the concrete cover. As for the values of the parameters in Table 1 for the steel cyclic model of Menegotto and Pinto [16], they can be determined either experimentally, if possible, or alternatively the values of Table 1 can be taken as suitable for the most common steel types of the daily practice, as mentioned in Section 3.

8. Conclusions

A new model is proposed for the inelastic behavior of RC-beam elements under biaxial bending with axial load. The model is suitable for slender beam elements without significant influence of the bond-slip phenomenon. It can also be used for elements with arbitrary cross-section shapes, which is one of its main targets.

The model uses a polygonization technique for discretizing the cross-sections into polygons. This polygonization initially appears as a Delaunay grid of triangles, and then it is transformed to a Voronoi diagram of control points. The latter act as fibers, similarly to the classic fiber models. The grid of triangles is used for the integration of concrete-compressive stresses over the compression zone of the cross-section, while the Voronoi diagram is used for the computation of its stiffness matrix.

This polygonization technique in combination with the mixed-formulation method of Taucer et al. [5] proved to be very efficient for inelastic analyses of RC specimens or framed structures, overcoming the usual numerical problems which occur in the classic fiber models when used with relatively coarse-fiber grids. Thus, the low computational cost of the model is due to the small degree of dependence on the number of the required critical control points that form the Delaunay triangularization.

Application of the model to various examples from the literature can be found in Part II of the present research work. Comparison between experimental and analytical results show very good to excellent agreement.

Author Contributions: Conceptualization, D.K.S. and M.G.S.; methodology, D.K.S. and M.G.S.; MINOS FEM Code software, v3 [23], M.G.S. and D.K.S.; validation, D.K.S.; formal analysis, D.K.S.; investigation, D.K.S. and M.G.S.; resources, D.K.S. and M.G.S.; data curation, D.K.S.; writing—original draft, D.K.S.; writing—review and editing, D.K.S. and M.G.S.; visualization, D.K.S. and M.G.S.; supervision, M.G.S.; project administration, M.G.S. All authors have read and agreed to the published version of the manuscript.

Funding: This research received no external funding.

Institutional Review Board Statement: Not applicable.

Informed Consent Statement: Not applicable.

Data Availability Statement: The raw data supporting the conclusions of this article will be made available by the authors on request.

Conflicts of Interest: The authors declare no conflicts of interest.

Appendix A

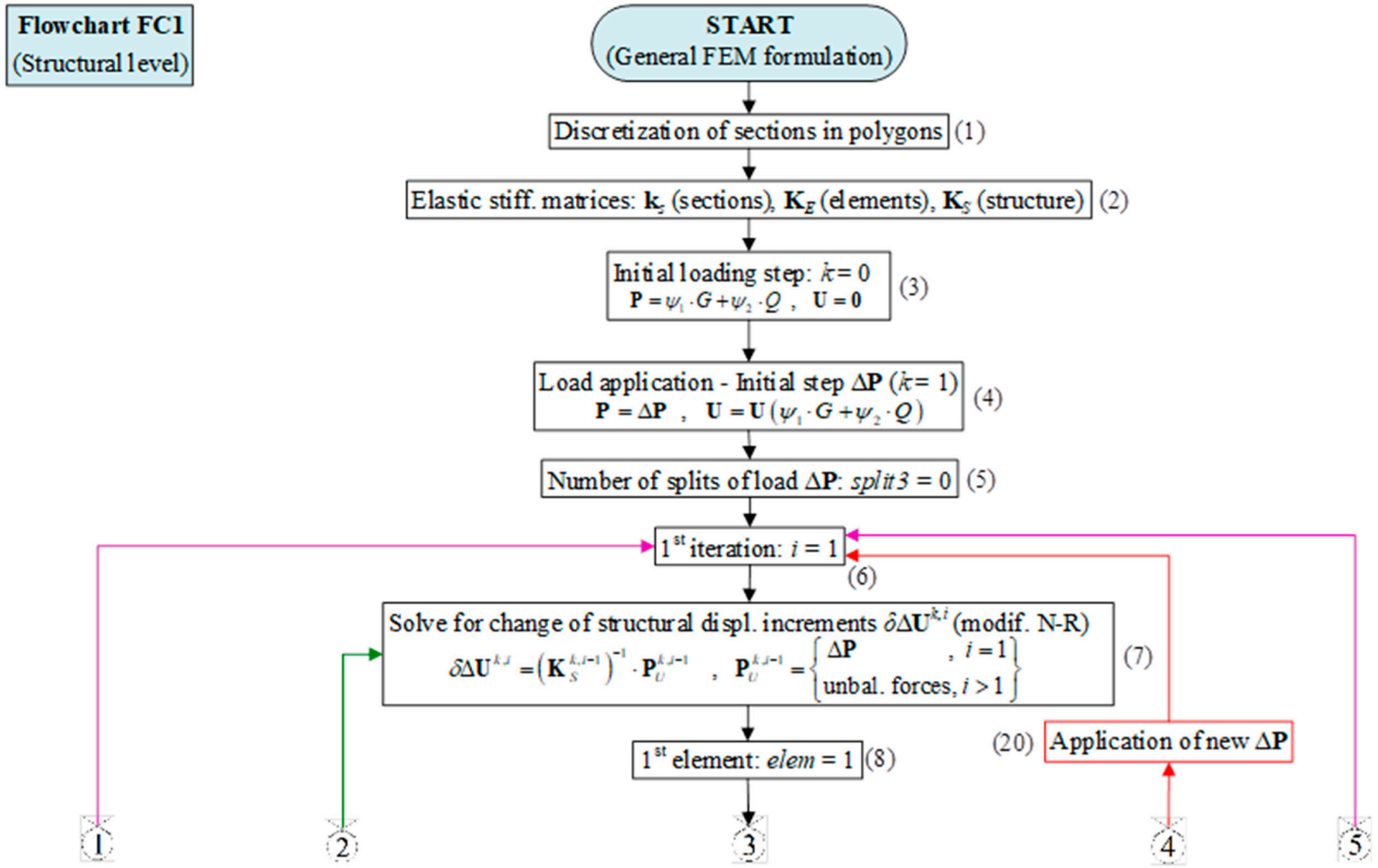

Figure A1. *Cont.*

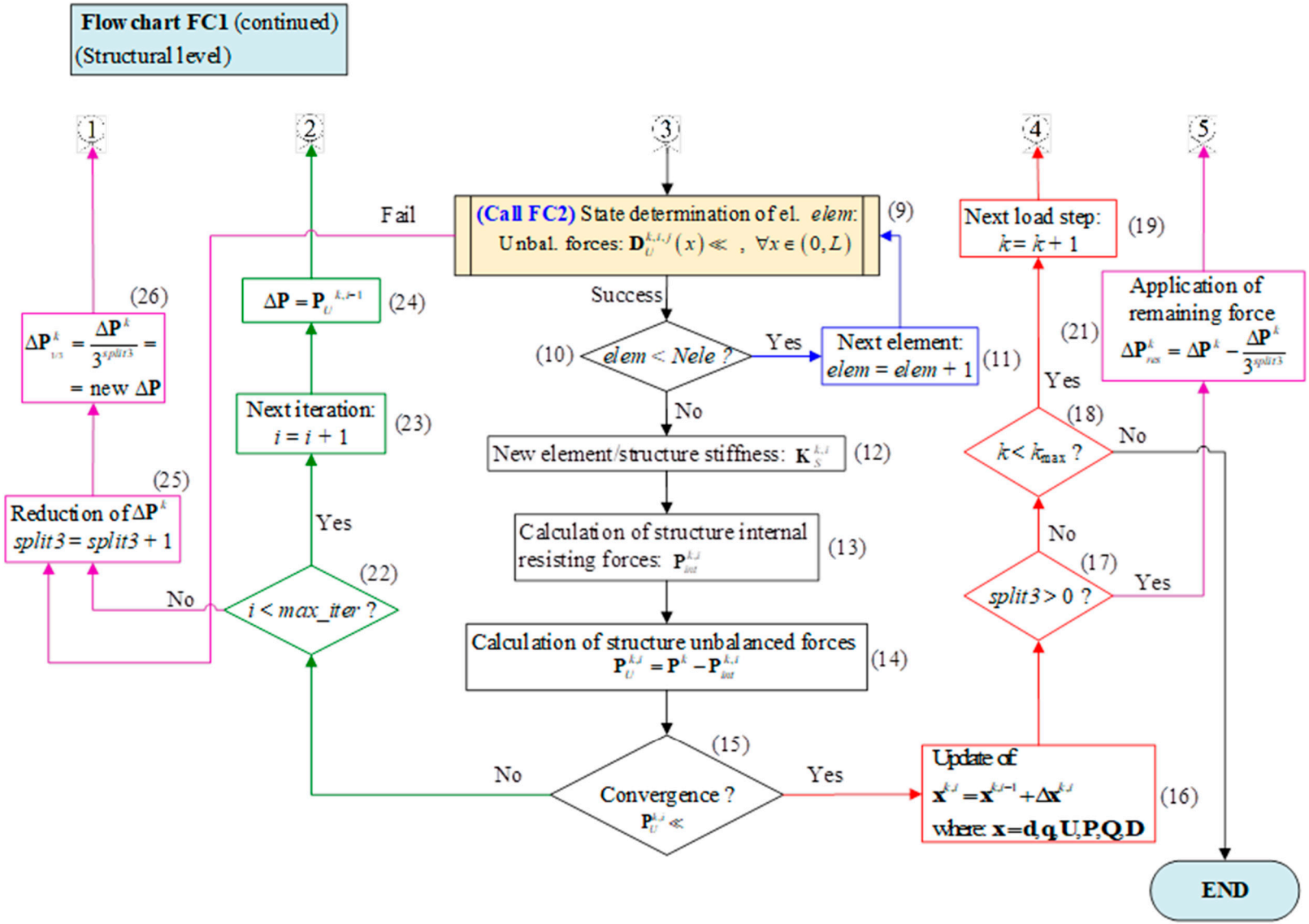

Figure A1. Flowchart FC1. Structural level.

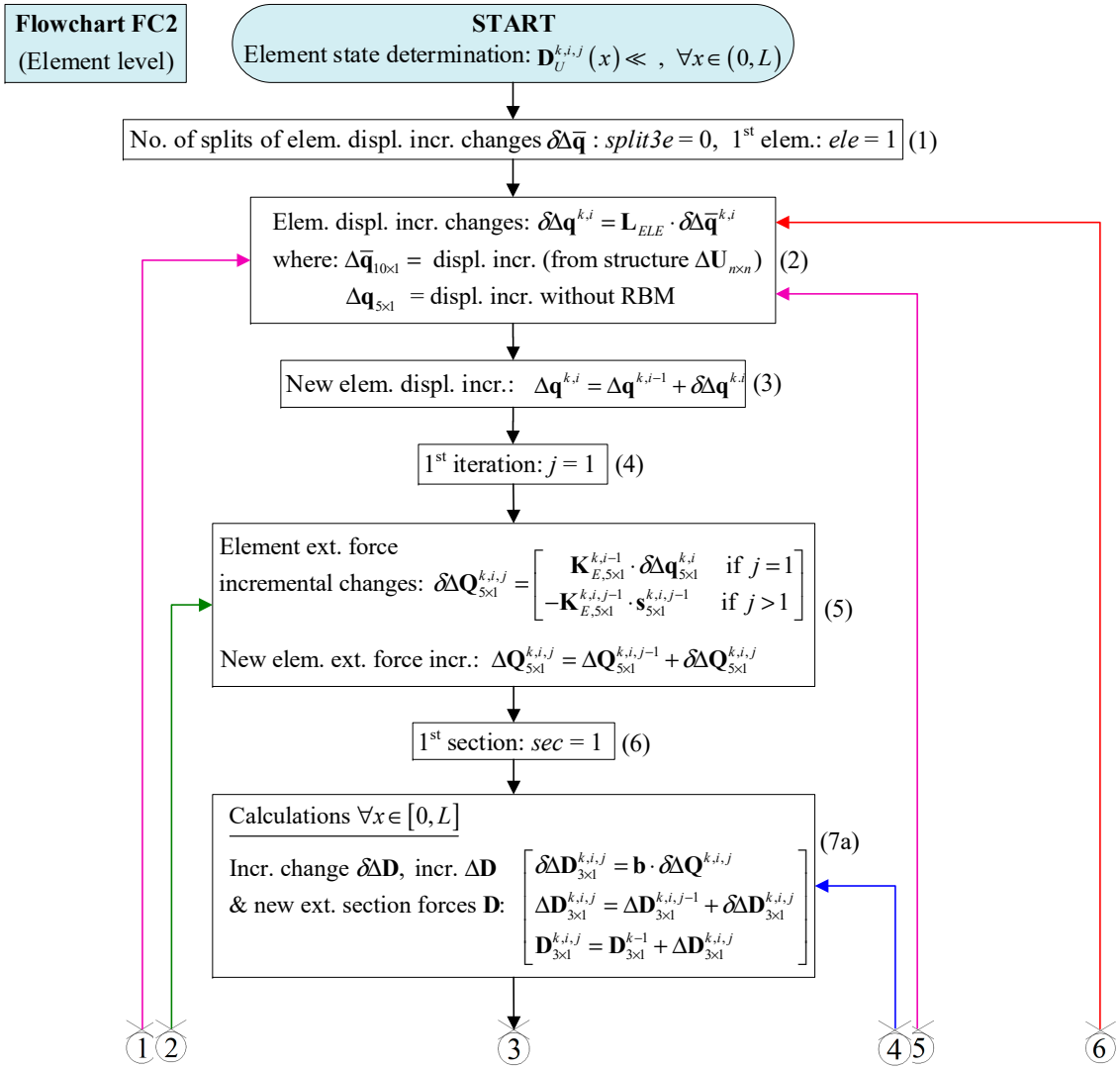

Figure A2. *Cont.*

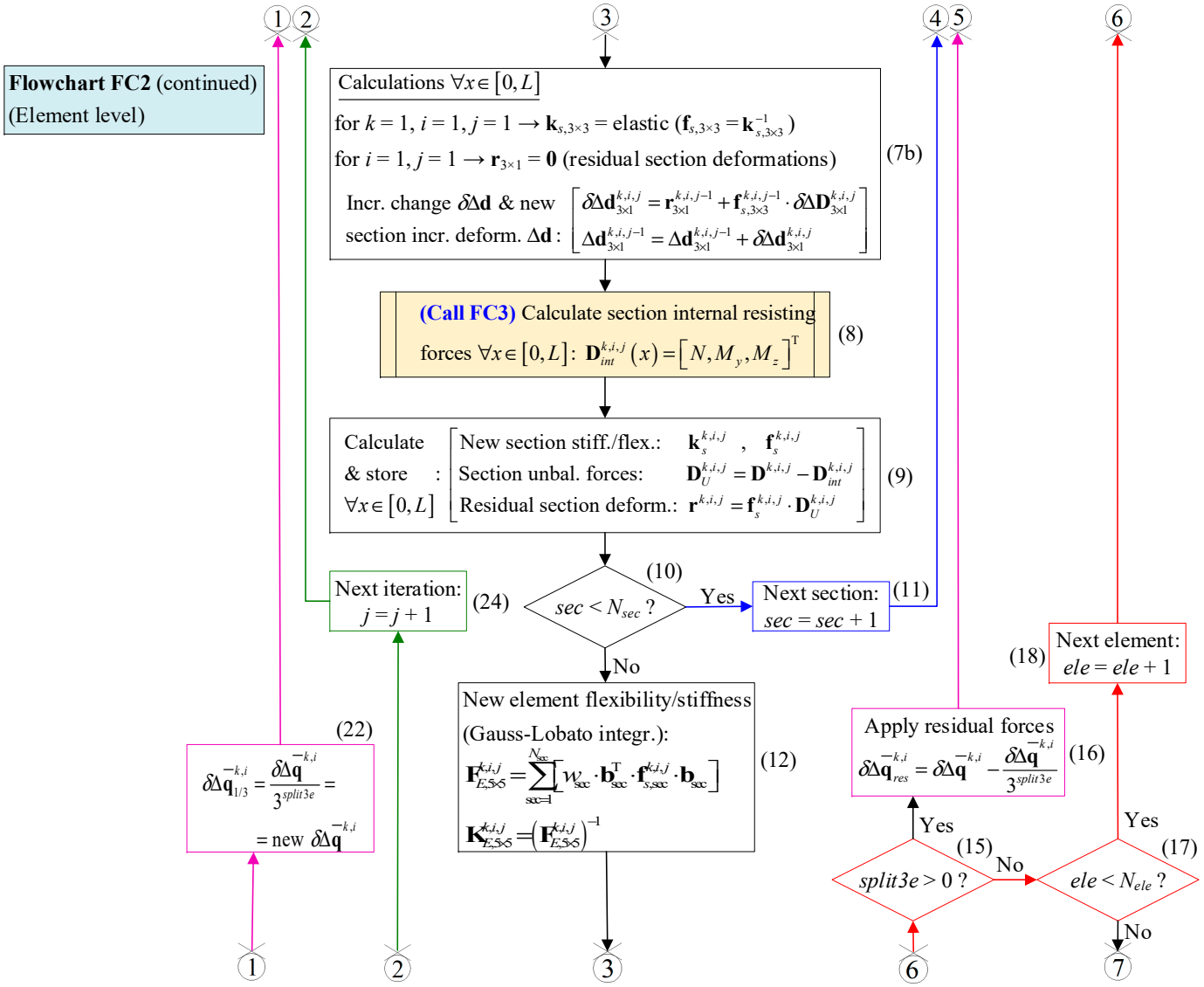

Figure A2. *Cont.*

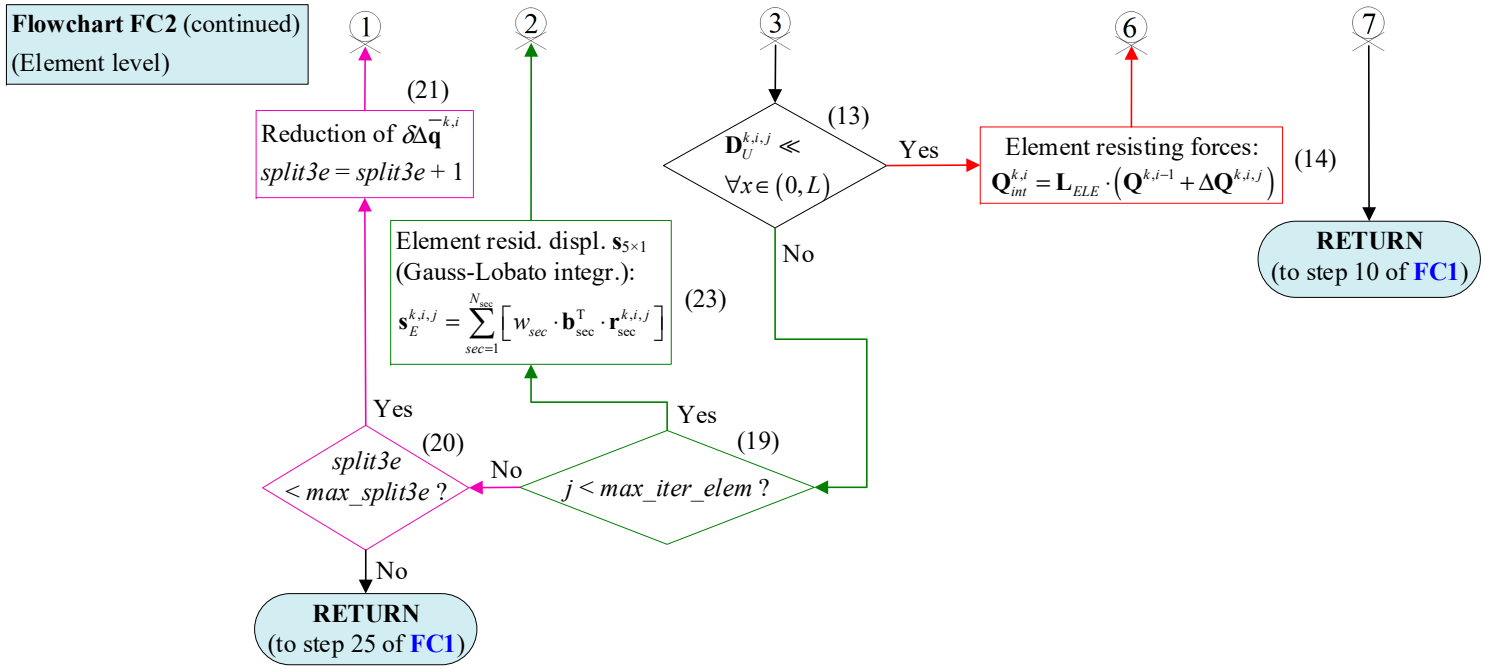

Figure A2. Flowchart FC2. Element level.

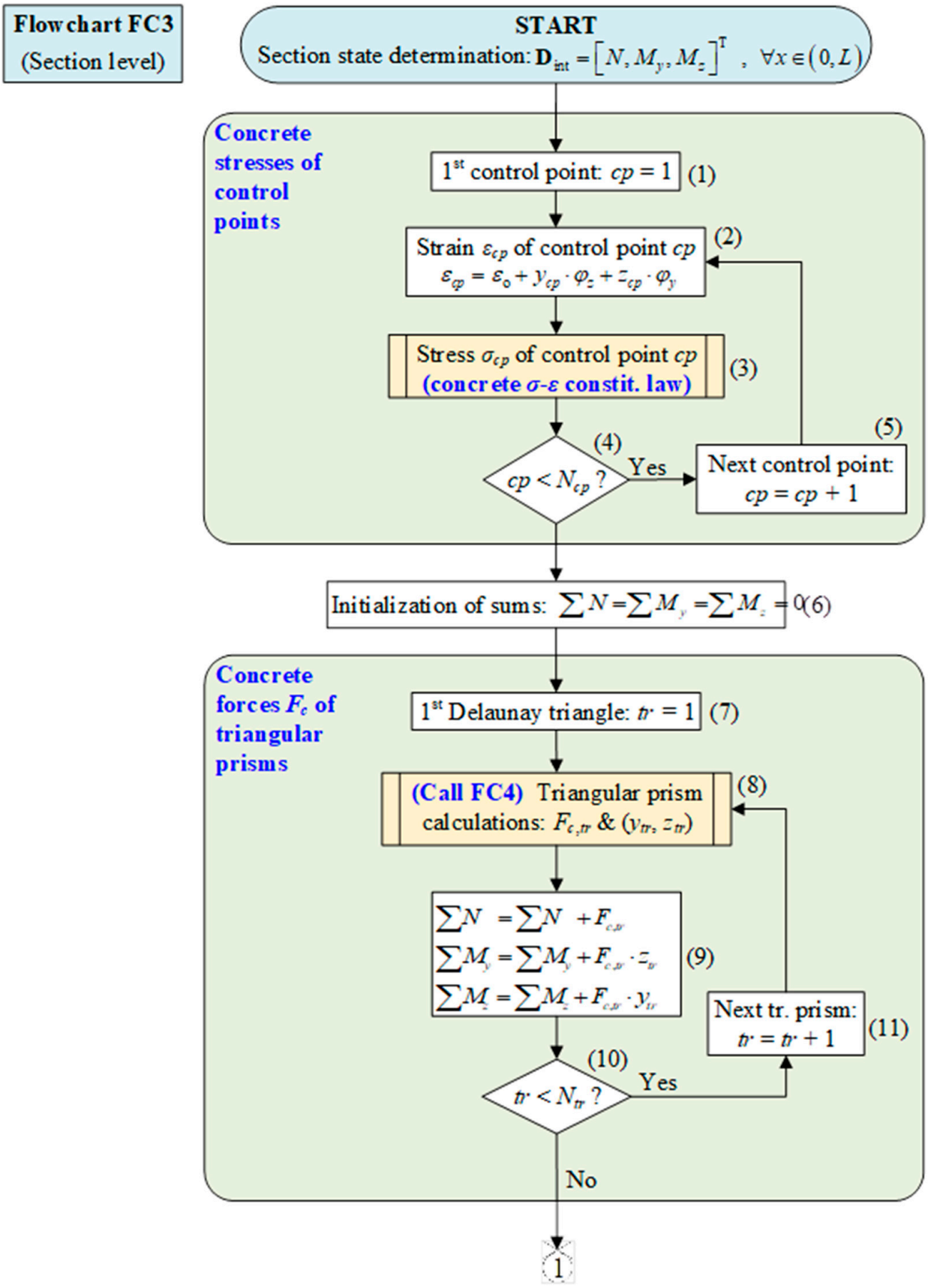

Figure A3. *Cont.*

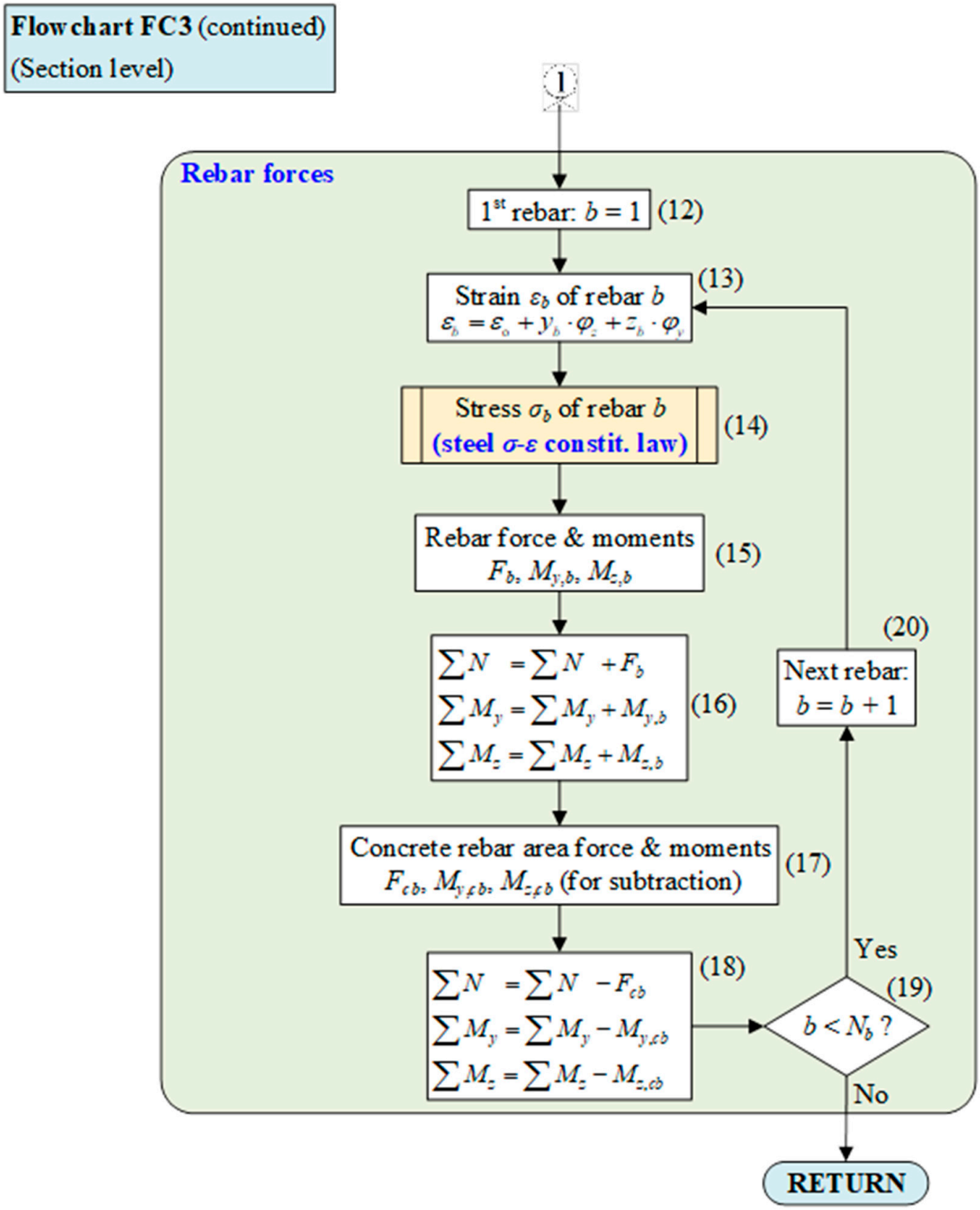

Figure A3. Flowchart FC3. Section level.

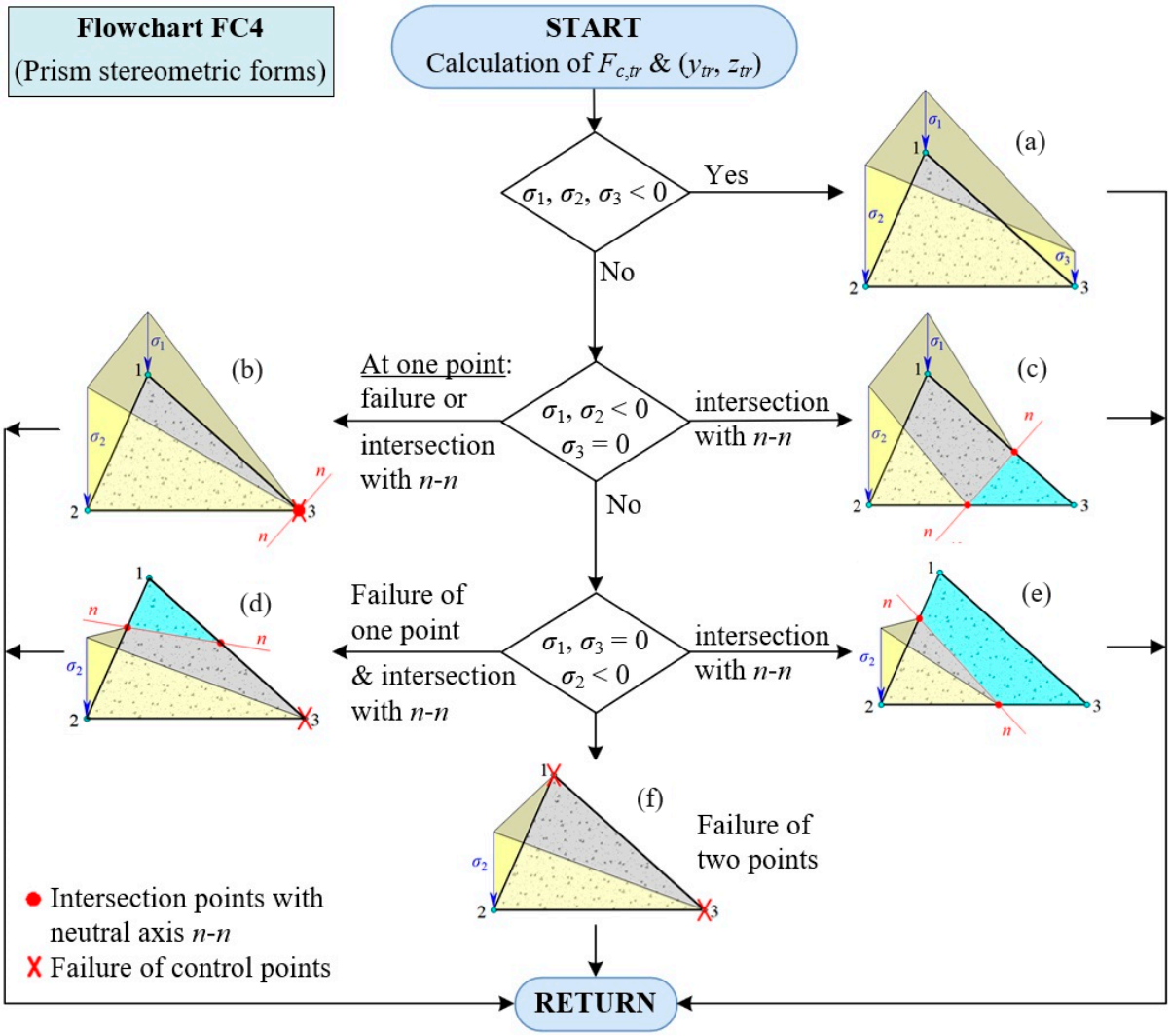

Figure A4. Flowchart FC4. (**a**–**f**) are the six possible prism stereometric forms.

References

1. Hellesland, J.; Scordelis, A. Analysis of RC bridge columns under imposed deformations. In *IABSE Colloquium*; IABSE Publ: Delft, The Netherlands, 1981; pp. 545–559.
2. Mari, A.; Scordelis, A. *Nonlinear Geometric Material and Time-Dependent Analysis of Three-Dimensional Reinforced and Pre-stressed Concrete Frames*; Research Report: SESM Report 82/12; Department of Civil Engineering, University of California: Berkeley, CA, USA, 1984.
3. Mahasuverachai, M.; Powell, G.H. *Inelastic Analysis of Piping and Tubular Structures*; Report UCB/EERC 82–27; Earthquake Engineering Research Center, University of California: Berkeley, CA, USA, 1982.
4. Zeris, C.A.; Mahin, S.A. Behavior of reinforced concrete structures subjected to biaxial excitation. *J. Struct. Eng.* **1991**, *117*, 2657–2673. [CrossRef]
5. Taucer, F.; Spacone, E.; Filippou, F.C. *A Fiber Beam-Column Element for Seismic Response Analysis of Reinforced Concrete Structures*; Report UCB/EERC 91-17; Earthquake Engineering Research Center, University of California: Berkeley, CA, USA, 1991.
6. Spacone, E.; Ciampi, V.; Filippou, F.C. *A Beam Element for Seismic Damage Analysis*; Report UCB/EERC-92/07; Earthquake Engineering Research Center, University of California: Berkeley, CA, USA, 1992.
7. Spacone, E.; Filippou, F.C.; Taucer, F.F. Fibre beam-column model for non-linear analysis of RC frames: Part I. Formulation. *Earthq. Eng. Struct. Dyn.* **1996**, *25*, 711–725. [CrossRef]
8. Spacone, E.; Filippou, F.C.; Taucer, F.F. Fibre beam-column model for non-linear analysis of RC frames: Part II. Applications. *Earthq. Eng. Struct. Dyn.* **1996**, *25*, 727–742. [CrossRef]
9. Monti, G.; Spacone, E. Reinforced concrete finite element with bond-slip. *J. Struct. Eng. ASCE* **2000**, *126*, 654–661. [CrossRef]
10. Kagermanov, A.; Ceresa, P. 3D fiber-based frame element with multiaxial stress interaction for RC structures. *Adv. Civil Eng.* **2018**, *2018*, 8596970. [CrossRef]

11. Bairan, J.; Mari, A. Multiaxial-coupled analysis of RC cross-sections subjected to combined forces. *Eng. Struct.* **2007**, *29*, 1722–1738. [CrossRef]
12. Kashani, M.; Lowes, L.; Crewe, A.; Alexander, N. Nonlinear fiber element modeling of RC bridge piers considering inelastic buckling of reinforcement. *Eng. Struct.* **2016**, *116*, 163–177. [CrossRef]
13. Sfondylis, D.K. Development of Generalized Nonlinear Beam Element Models for Slender RC Members. Ph.D. Thesis, University of Patras, Patras, Greece, 2020.
14. Martínez-Rueda, J.E.; Elnashai, A.S. Confined concrete model under cyclic load. *Mater. Struct.* **1997**, *30*, 139–147. [CrossRef]
15. Mander, J.B.; Priestley, J.N.; Park, R. Theoretical stress-strain model for confined concrete. *J. Struct. Eng.* **1998**, *114*, 1804–1826. [CrossRef]
16. Menegotto, M.; Pinto, P.E. *Method of Analysis for Cyclically Loaded RC Plane Frames including Changes in Geometry and Non-Elastic Behaviour of Elements under Combined Normal Force and Bending*; Preliminary Report; International Association of Bridge and Structural Engineering: Zürich, Switzerland, 1973; Volume 13, pp. 15–22.
17. Filippou, F.C.; Popov, E.P.; Bertero, V.V. *Effects of Bond Deterioration on Hysteretic Behavior of Reinforced Concrete Joints*; Report EERC 83-19; Earthquake Engineering Research Center, University of California: Berkeley, CA, USA, 1983.
18. Mazzoni, S.; McKenna, F.; Scott, M.H.; Fenves, G.L.; Mahin, S.A. *Opensees Command Language Manual*; Technical Report, The Open System for Earthquake Engineering Simulation; University of California: Berkeley, CA, USA, 2006.
19. Giuffrè, A.; Pinto, P.E. Il comportamento del cemento armato per sollecitazioni cicliche di forte intensità. *G. Genio Civ.* **1970**, *5*, 391–408.
20. Yassin, M.H.M. Nonlinear Analysis of Prestressed Concrete Structures under Monotonic and Cyclic Loads. Ph.D. Thesis, University of California, University of California, Berkeley, CA, USA, 1994.
21. Zalik, B.; Clapworthy, G.A. Universal trapezoidation algorithm for planar polygons. *Comput. Graph.* **1999**, *23*, 353–363. [CrossRef]
22. Sfakianakis, M.G. Biaxial bending with axial force of reinforced, composite and repaired concrete sections of arbitrary shape by fiber model and computer graphics. *J. Adv. Eng. Softw.* **2001**, *33*, 227–242. [CrossRef]
23. Sfakianakis, M.G. *MINOS-2D & 3D–A FEM General Purpose Computer Program for Nonlinear Analysis of Structures*; Theory Manual & User's Guide; University of Patras: Patras, Greece, 2001.
24. *KAN.EPE.-2017*; Greek Code for Interventions in RC Buildings. Earthquake Planning and Protection Organization (OASP): Athens, Greece, 2017.

Disclaimer/Publisher's Note: The statements, opinions and data contained in all publications are solely those of the individual author(s) and contributor(s) and not of MDPI and/or the editor(s). MDPI and/or the editor(s) disclaim responsibility for any injury to people or property resulting from any ideas, methods, instructions or products referred to in the content.